Spectral filter design based on in-field hyperspectral imaging and machine learning for mango ripeness estimation

Salvador Gutiérrez[a,*], Alexander Wendel[b], James Underwood[b]

[a] *Instituto de Ciencias de la Vid y del Vino (University of La Rioja, CSIC, Gobierno de La Rioja), Finca La Grajera, Ctra. Burgos Km. 6, 26007 Logroño, Spain*

[b] *Australian Centre for Field Robotics, The Rose Street Building J04, The University of Sydney, NSW 2006, Australia*

Abstract

Hyperspectral imaging (HSI) is a powerful technology already used for many objectives in agriculture. Applications include disease monitoring, plant phenotyping, yield estimation or fruit composition and ripeness. However, the cost of hyperspectral sensors is typically an order of magnitude higher than simpler RGB cameras, which can be prohibitive. Given that in HSI processing the spectral data often contains redundancies, the full spectra are not always required for a specific application and there is an opportunity to design a lower cost multi-spectral sensing system by dimensionality reduction. In past work, HSI dimensionality reduction has been applied in the form of band selection to achieve faster computation times. If, however, the objective is to design a lower cost multi-spectral camera system, band selection is poorly suited because real-world sensor and optical filter responses do not typically replicate the individual bands of a hyperspectral sensor. The objective of this paper is to develop a new methodology for filter selection by simulating several imaging devices with different real-world optical filters, to use a high cost HSI device to design a lower cost multi-spectral solution for a specific application. In this paper, we apply the technique to the specific task of mango fruit maturity estimation (dry matter), which was recently shown to be possible using HSI. Mango HSI acquired under field conditions from an UGV was used as input for the experiments. These involved the simulation of imaging devices, using support vector machines for modelling, and testing several filter combinations by brute force or optimisation with genetic algorithms. The mango prediction performance of the simulations was compared to the best performance obtained with full HSI data, which had an R^2 of 0.74. The best values came from the simulation of a four-sensor device with four distinct filters, achieving R^2 up to 0.69 for mango dry matter estimation. The results showed that genetic algorithms, when compared to brute force approaches, were able to obtain the best solution in an efficient way, and that a good performance for mango ripeness estimation can be achieved from the combination of four spectral filters that would allow to implement them into a low-cost, custom-made multi-spectral sensor. The methods exposed in this paper are more broadly applicable to applications beyond mango maturity estimation.

Keywords: filter selection, band selection, genetic algorithms, optimisation, field robotics, computer vision, hyperspectral, spectroscopy, dry matter

*Corresponding author

Email addresses: salvador.gutierrez@unirioja.es (Salvador Gutiérrez), a.wendel@acfr.usyd.edu.au (Alexander Wendel), j.underwood@acfr.usyd.edu.au (James Underwood)

1. Introduction

Hyperspectral imaging (HSI) is actively studied for many food and agricultural applications [31, 38]. HSI combines high spatial resolution imaging such as commonly done using simpler RGB cameras, with high spectral resolution more commonly used in spectroscopy. Because many physical properties can be derived from the analysis of the interaction between light and matter [36], HSI is useful for estimating traits or characteristics of visible objects. In the context of precision agriculture, recent studies have shown HSI applications for plant disease monitoring [41, 26, 29], phenotyping [3, 28, 20, 11] or fruit composition [6, 35, 43, 19], which have all been developed in laboratory and not field conditions. By contrast, publications describing in-field HSI applications are less common, but efforts in this area have been increasing recently. HSI has been manually acquired under field conditions for the segmentation of raspberry plants [49], and also mounted on phenotyping platforms [5]. Terrestrial vehicles for on-the-go HSI acquisition were also employed for varietal classification in grapevines [15] (manned platform), mango ripeness prediction [48] or yield estimation [16] at whole-orchard scale (unmanned platforms). Detailed studies also exist describing the technical details for using hyperspectral sensing on unmanned ground vehicles (UGVs) concerning illumination compensation [47] or extrinsic parameter calibration [46]. In agricultural applications, the high-resolution data gathering from HSI in both spectral (hundreds of channels) and spatial dimensions (especially when acquired at close range from ground vehicles) make this technology suitable for detailed in-field monitoring of crops. Nevertheless, hyperspectral cameras are typically more expensive than other sensing technologies. Additionally, it is known that spectral data—generally represented as vectors with several hundreds of variables (bands or channels)—suffers from high information redundancy, especially between adjacent bands [52]. Consequently, given the high cost and redundancy of HSI, the question arises, is it really necessary to use all the bands from spectral data, acquired at significant cost, or is it possible to obtain virtually the same information after dimensionality reduction? Simplification of the input could lead to options for lower cost sensor systems that are designed to match specific applications.

Spectral dimensionality reduction (from any kind of sources, not only limited to HSI) is a costly procedure due to its combinational complexity [50], especially if an exhaustive search is performed. For this reason, different machine learning metaheuristics are commonly used to optimise the selection of spectral bands. Some of these techniques include genetic algorithms (GAs) [30, 24, 32], particle swarm optimization [50, 53, 4] or ant colony optimisation [39, 13, 42]. Nevertheless, while most of the studies seek to provide a reduced selection of spectral bands, they lack one important factor: the channels they propose, regardless of their number, are individual and based on the original spectrum. If the acquisition of those specific channels is attempted to check its reproducibility, the only feasible way would be to use a spectral sensor capable of acquiring full high-resolution spectra that covers the selected wavelengths, and then isolate those specific individual datapoints. For example, nine and twelve different wavelengths for two datasets were selected in [23], while up to dozens of wavelengths were reported in [12] for endmember extraction in hyperspectral images. Specifically, in agricultural applications, in [30] the authors used GAs for band selection on soybean disease detection from HSI, reporting that six specific wavelengths maximised the performance for the desired task. A methodology for grapevine water status estimation based on near-infrared spectroscopy (NIR) was reported in [14], and, from Visible-NIR spectroscopy, selected five specific bands within a very narrow range between 700 and 800 nm that highly correlated with water content. For the same grapevine water status prediction goal, an older study [54] also reported good results when reducing the number of variables to 25 from full Vis-NIR spectra. While the results from these studies met their objective to reduce computational complexity in data processing, the same process cannot be readily applied to developing low-cost ad-hoc spectral sensors, particularly when dozens of bands have been selected.

Assuming that it is desired to build a multi-band spectral sensor after identifying a reduced set of narrow-band wavelengths using any of the methodologies described before, it would be very difficult to obtain measurements of those bands in any other way than using HSI and discarding the surplus data. This is due to manufacturing limitations in optical filter design and also because of the poor light signal-to-noise ratio (SNR) that is obtained when very narrow filters are employed. Several works on different methodologies for filter design have also reported these difficulties [21, 17, 18, 45]. In [34] and [51], the authors attempted the simulation of colour filters by optimising three, five and 10 filters in terms of amplitude, efficiency and/or SNR. Special attention should be paid to two papers on the practical implications of the development of cameras based on multi-spectral filter arrays (MSFA) [22, 25]. MSFA-based cameras are a useful option for the manufacturing of a multi-spectral camera with a few channels (typically three to six) that takes full snapshot. The authors in [22] provide a review on multi-spectral acquisition systems, and report the development of a custom made spectral device. The authors display the difficulties of using the results from a filter optimisation process to build a custom-made camera, because of the current limitations that exist in the manufacturing processes. In [25], the authors performed a simulation of a MSFA-based imaging sensor for spectral reconstruction, focusing on how to optimise the response of filter arrays and demosaicing. All these studies are good examples of how it is possible to build multi-spectral cameras, and they manifest that the theoretical response of selected wavelengths (by optimisation or other means) is not easy to reproduce.

This paper develops a new methodology for filter selection using machine learning techniques to fill a gap between the two exposed approaches: the broadly studied wavelength band-selection by optimisation; and considering the design and usage of optical filters instead of selecting specific bands. Using HSI data acquired from an UGV for the purpose of mango ripeness estimation, the methodology developed here simulates the potential for lower cost multi-spectral solutions to the same problem, by optimising the selection of lower cost camera/filter combinations. The prediction of dry matter (DM) is a desirable goal in mango industry, as it is considered an important indicator for fruit ripeness [44]. Proximal HSI has already been demonstrated to be an effective tool for the automatic estimation of DM in mango orchards [48], hence we sought to understand the trade-off necessary to develop a multi-spectral solution (*e.g.*, with the need of reducing the spectral dimensionality) while maintaining a good response in prediction. The underlying approach could also be adapted for specific objectives beyond ripeness estimation.

2. Materials and methods

The analysis performed in this study used as input the same data obtained in [48], for mango ripeness estimation, validating the DM content with a hand-held NIR spectrometer already tested in other works [2, 7]. HSI on mangoes was performed under field conditions from a UGV and used to simulate expected performance with single and multi-spectral sensor systems, with a view to cost reduction. The optimal single-sensor solution identified from simulation was also verified with the matching real-world (non-simulated) device.

The methodological pipeline followed in this study is displayed in Fig. 1. The simulated multi-spectral sensors were: 1) a device with one monochrome camera sensor and one filter in front of it (Fig. 1a), 2) a device with one RGB sensor and one filter in front of it (Fig. 1b), and finally 3) a device with four different monochrome sensors (a typical configuration in retail multi-spectral cameras), each one of them with a different filter (Fig. 1c). Filter responses were obtained by multiplying the reflectance spectra (from HSI and after correction) by the filter transmittance profile, and then integrating. Two different filter pools were tested: 1) theoretical, parametrically defined filters and 2) actual commercial off-the-shelf (COTS) filters with filter responses defined in commercial datasheets (Fig. 1d). The filter selection optimisation was performed by GAs, which we propose as a more generally computationally tractable solution, while also verified by a more expensive brute force approach (Fig. 1e).

The first device (Fig. 1a), an RGB sensor with one filter (Fig. 1b), was simulated by testing all the filters from the COTS pool using SVMs in a brute force approach. The same flow was followed for the device with a monochrome camera sensor, the only difference being that simple linear regression was used for modelling due to the one-dimensional input that is generated. Finally, data were obtained from a real camera with the optimal IR cut filter identified and compared to the simulation of an RGB camera (from red, green and blue colour bands recorded by the hyperspectral camera) with the same IR cut filter. This comparison was used to validate the accuracy of the simulated filters.

Models from RGB data were also developed and compared with real RGB imaging, to verify the validity of the simulation. The filter selection for the four-sensor device (Fig. 1c) was performed by GAs two times: one from parametric filters and one from COTS filters. All permutations of filter combinations were tested using a brute force approach, to validate the proposed GA approach.

2.1. Data collection

Data acquisition was carried out in a mango orchard (*Mangifera indica L.*) located in Bundaberg, Queensland, Australia, on the 6th of December, 2017. Seventy-eight mango fruits were selected assuring a large variability in DM values. Fig. 2 shows a histogram of the mango DM values, ranging from less than 10 to 21.5% m/m ($\mu = 12.98\%\ w/w, \sigma = 2.39\%\ w/w$). Mangoes were distributed in five fruit trays for spectral acquisition (Fig. 3b).

A hand-held NIR spectrometer (Felix F-750, Felix Instruments Inc., Camas, USA) was employed as reference method for DM content. This device uses a Zeiss MMS1 NIR sensor with a spectral range from 400 to 1100 nm, having pixel and optical resolutions of 10 and 3.3 nm respectively. Radiometric calibration is performed by referencing on every measurement from an internal halogen lamp and background illumination. The spectrometer was calibrated prior to use following the instructions from the manufacturer [10], with validation $R^2 = 0.95$, and RMSE = 0.56% w/w. The performance of this instrument for mango DM estimation was already proven by other authors in different experiments [2, 7].

A general purpose unmanned ground vehicle (UGV), developed at the Australian Centre for Field Robotics and called "Shrimp", was used for HSI and RGB image data acquisition (Fig. 3). The vehicle was equipped with a Resonon Pika II Vis-NIR hyperspectral line-scan camera (Resonon, Inc., Bozeman,

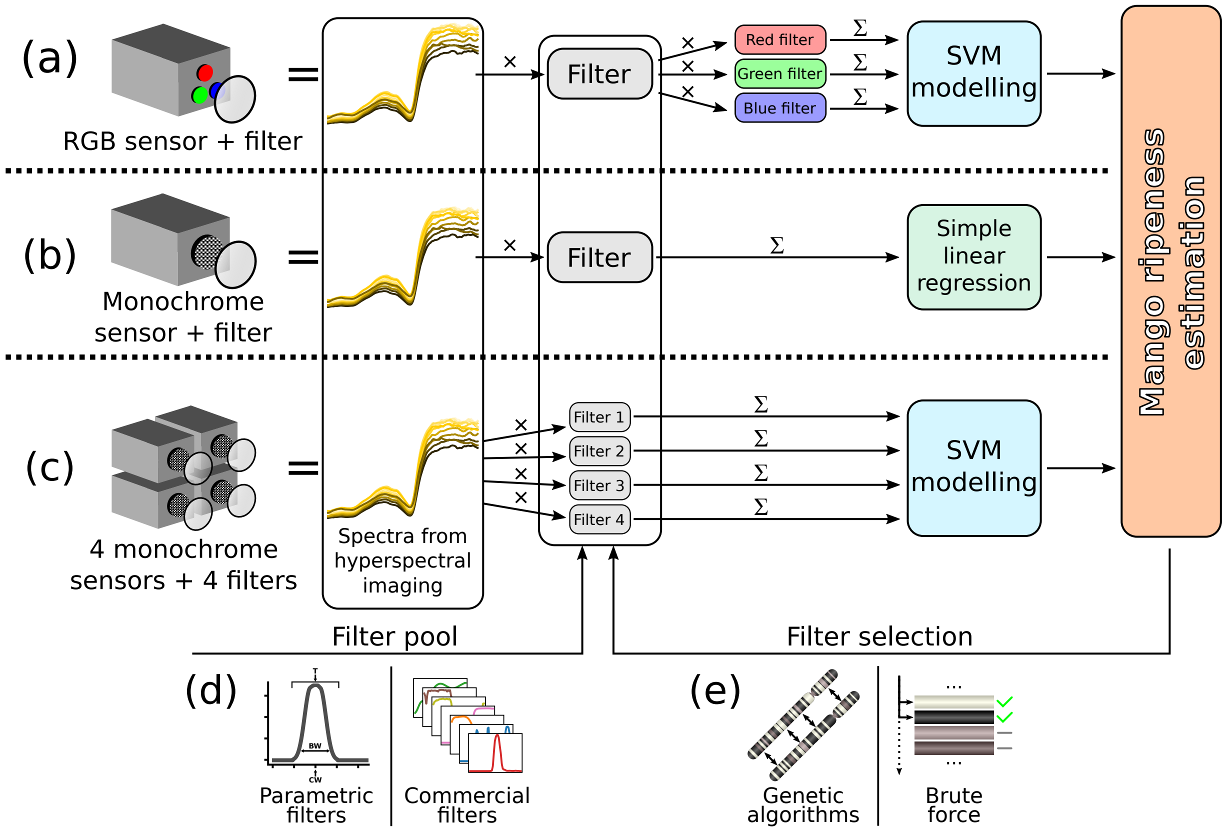

Figure 1: The simulation of three different kinds of lower cost single and multi-spectral sensors for ripeness estimation was carried out from HSI on mangoes performed under field conditions from a UGV. The simulated spectral devices were: an RGB sensor with one filter in front of it (a), a monochrome camera with one filter in front of it (b) and finally a system of four monochrome sensors (a typical configuration in retail multi-spectral cameras), each with a different filter (c). Filters were selected from two different pools (d) and using two different selection methodologies (e).

USA), shown in Fig. 3a, that has 648 spatial dimensions (pixels) and 244 spectral datapoints with a depth of 12 bits and covering the Vis-NIR range from approximately 390 to 890 nm (spectral resolution of 2 nm). HSI data acquisition was configured to be performed at different times and to measure both mango sides, after manual rotation of each fruit in the trays. Several illumination reference panels (QPcard 102) were placed adjacent to the trays for radiometric calibration (Fig. 3b). At the same time as HSI scanning, an RGB camera was used for image acquisition of the fruit in the trays. A Prosilica GT3300C camera (Allied Vision Technologies GmbH, Stadtroda, Germany) was employed (Fig. 3a), with a NIR cut filter SP700[1] mounted [27], and in synchronisation with four Excelitas MVS-5000 strobe lights (Excelitas Technologies Corp., Waltham, USA), as described in [37]. The system has been demonstrated to be effective for scanning ripeness in whole orchards [48, 37], but for this work it was used to scan the trays seen in Fig. 3b.

Illumination compensation was applied to the hyperspectral data. In the first place, the raw HSI data

[1]The SP700 is a relatively standard IR cut filter as commonly used in standard RGB cameras. This filter discards the small NIR sensitivity present in common RGB filters (small heap starting from around 800 nm in the blue line in Fig. 4.)

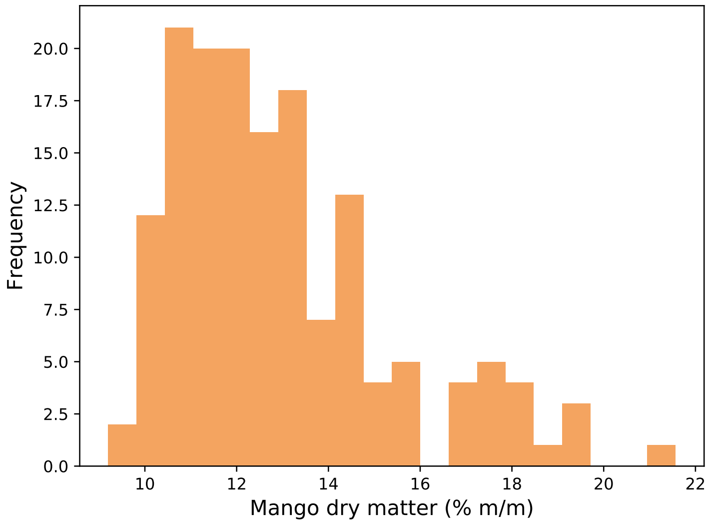

Figure 2: Histogram of the dry matter values from the mango samples measured by the hyperspectral camera.

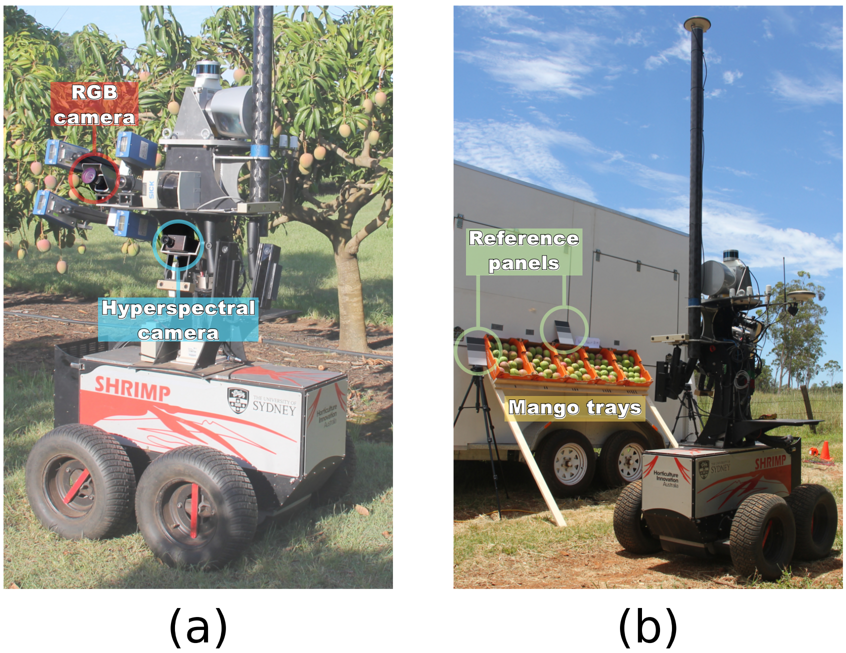

Figure 3: Picture of the unmanned ground vehicle (UGV) and the RGB and hyperspectral cameras (a) and the UGV during data acquisition upon the mango trays (b).

was transformed to at-sensor radiance using the following formula from [40]:

$$\mathbf{l}_{\mathrm{s}}(\lambda) = \frac{\mathbf{dn}_{\mathrm{s}}(\lambda) - \mathbf{dn}_{\mathrm{sdc}}(\lambda)}{\mathbf{dn}_{\mathrm{ff}}(\lambda) - \mathbf{dn}_{\mathrm{ffdc}}(\lambda)} \mathbf{l}_{\mathrm{ff}(\lambda)} \tag{1}$$

where $\mathbf{dn}_{\mathrm{s}}(\lambda)$ is raw digital number (DN) values of the sample s at a wavelength λ, $\mathbf{dn}_{\mathrm{sdc}}(\lambda)$ is DN values of dark current; while $\mathbf{dn}_{\mathrm{ff}}(\lambda)$ and $\mathbf{dn}_{\mathrm{ffdc}}(\lambda)$ are flat field DN values acquired using an integrating sphere and corresponding dark current, respectively. $\mathbf{l}_{\mathrm{ff}(\lambda)}$ corresponds to the internal radiance values of the integrating sphere. Finally, after applying the "LOGSEP" method described by [47] and [8], the values were converted to reflectance. This pre-processing was carried out to account for the effects of non-uniform lens transmittance and sensor quantum efficiency. For further details on data collection and spectral preprocessing, the reader is referred to [47] and, especially, to [48], as mango DM estimation using ground-based HSI is presented in that paper, and the same dataset was used for filter selection in the present study.

2.2. Dataset building and model development

Having 78 mangoes and two scanned sides per fruit, the final dataset comprised a total of 156 samples. Each sample contained the full average spectrum from the visible side of the mango and its corresponding DM value as measured with the hand-held spectrometer described in Section 2.1.

Except where indicated otherwise, all the models developed in this study were trained using Epsilon-Support Vector Machines (ε-SVMs) as regressors from the Support Vector Regression (SVR) implementation in scikit-learn 0.19.1 [33], using the default values provided by the library for the hyperparameters.

The selection of ε-SVMs and the hyperparameter values set was carried out after intensive supervised testing of different algorithms and hyperparameter configurations upon the original 156-samples dataset, and based on our knowledge and experience using machine learning techniques for this kind of data input. We want to highlight that, within the spectral filter design methodology described in this paper, the selection of an adequate classificator or regressor depends on the target problem (in our case, DM estimation from HSI), and other methodologies may be applied.

Models were validated using five iterations of 5-fold cross validation (CV). Each one of the CV iterations used a different random number generator seed for fold splitting. Still, the same five seeds were used at each model development in this study to ensure that performance differences are due only to the input used, not the random distribution of the samples in the folds.

2.3. Filter selection

2.3.1. RGB and monochrome sensors

The monochrome device was simulated by testing all the filters from a pool of 96 COTS filters from MIDOPT [27], using a brute force approach. The list of model numbers can be found in Table 1. Filter data specifications—transmission data within the range of the hyperspectral camera used in this study—were obtained from the manufacturer web-site [27]. When using one filter in a monochrome device, only one intensity value is produced per pixel. Therefore, a simple linear regression between this intensity and mango DM was used for modelling.

A device with one RGB sensor and one filter in front of it was simulated in order to see how filtered RGB imaging is correlated with DM content in mangoes. From the HSI spectra, their RGB information (red, green and blue channels) was extracted using the quantum efficiency data from the Prosilica GT3300C (Fig. 4), provided by the manufacturer in [1]. The three quantum efficiency profiles were normalised to the unit to be used as the RGB sensitivity values, and then applied separately to the HSI raw spectra. Afterwards,

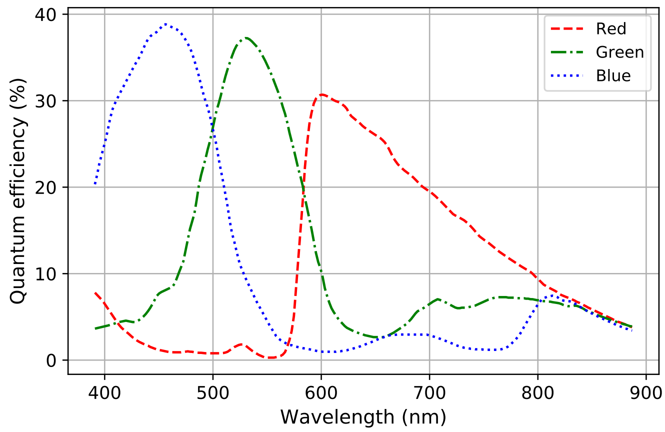

Figure 4: Quantum efficiency of the RGB filters assembled in the Prosilica GT3300C [1]. These filters were used to simulate a expected response from the hyperspectral images.

as in the monochrome device, all 96 COTS filters were tested in a brute force approach, applying each one of them to the three RGB channels.

Mango ripeness estimation from RGB was carried out for both HSI ($\mathrm{RGB}_{\mathrm{HSI}}$) and real Prosilica RGB imaging ($\mathrm{RGB}_{\mathrm{RGB\text{-}Camera}}$). This was tested as data was also available from real (not simulated) RGB camera with a MIDOPT IR cut filter, and these were compared to the simulated counterpart to validate the simulation approach.. Additionally, to test how well the RGB information from HSI was extracted (using the filters in Fig. 4), the correlation between $\mathrm{RGB}_{\mathrm{HSI}}$ and $\mathrm{RGB}_{\mathrm{RGB\text{-}Camera}}$ was tested after transformation from the RGB to the HSV (hue, saturation, value) colour space.

2.3.2. Four monochrome sensors

A device with four different monochrome sensors, each one of them with a different filter, was simulated, as this is a typical configuration in low-cost, retail multi-spectral cameras. Two independent pools were used for filter selection. The first pool was generated from parametric (hypothetical) filters, by fine tuning the corresponding parameters. The transmittance for each filter was generated from a normal distribution (with maximum in 1) defined by: its central wavelength in nm ($\mathrm{C}_N \in [390, 890]$); its bandwidth in nm ($\mathrm{B}_N \in [6, 492]$); and the type of filter ($\mathrm{T}_N \in \{\mathrm{bandpass}, \mathrm{longpass}, \mathrm{shortpass}\}$). Each filter is individually applied to the raw average spectra from the HSI data of each mango, obtaining four scalars representing the four filter responses. Therefore, the goal was to select the best four parametric filter combination that maximise the DM prediction capability.

The second filter pool was built from the same 96 COTS filters described in Section 2.3.1. The advantage to do this is that these filters are known to be feasible to construct and easy to obtain, whereas there is no guarantee that the optimal parametric filters would be practical. The goal again was to select the best four COTS filter combination that maximise the DM prediction capability.

Therefore, for each filter pool, two optimisation problems were defined. For parametric filters:

$$\arg\max_{P} f(\mathrm{C}_1, \mathrm{B}_1, \mathrm{T}_1, \mathrm{C}_2, \mathrm{B}_2, \mathrm{T}_2, \mathrm{C}_3, \mathrm{B}_3, \mathrm{T}_3, \mathrm{C}_4, \mathrm{B}_4, \mathrm{T}_4) \tag{2}$$

where f and is a fitness function that, given the 12 parameters (to define four filters), returns the R^2 score after applying the four filters to the HSI dataset and validating the models as described in Section 2.2.

For COTS filters:

$$\arg\max_{P} g(\mathrm{F}_1, \mathrm{F}_2, \mathrm{F}_3, \mathrm{F}_4) \tag{3}$$

where g is a fitness function that, given four different filters F_N, returns the R^2 score (for regression to dry matter) after applying them to the HSI dataset and validating the models as described in Section 2.2. Further details about the algorithms implementing the f and g functions can be found in Supplementary Material.

Although, by definition, C_N and B_N are real numbers expressed in nm, their values are represented as integers by the data from the HSI camera hardware, because of the integer binning in the spectral dimension (indices in an array). This, along with the fact that T_N and F_N are categorical variables, makes f and g non-continuous functions. For this reason, optimisation techniques based on derivatives or gradients cannot be used. A CHC-based genetic algorithm [9] was implemented for the parameter optimisation of f and g within the ranges defined for each variable. CHC algorithm (cross-generational elitist selection; heterogeneous recombination; cataclysmic mutation) is capable of providing a wide solution exploration—by keeping relatively small individual populations frequently reinitialised—while still maximising exploitation within a population.

CHC starts by setting a population of M individuals randomly initialised and a convergence value δ of $\frac{|P|}{4}$. At each iteration, $M/2$ crossovers are performed by randomly picking two parents (without replacement) and, if there is enough genetic difference between them (incest prevention), performing a half uniform crossover [9]. The best M individuals from the offspring and the original population are selected, and the cycle is repeated. If no offspring was generated, δ is decreased by one. If $\delta < 0$, the population is removed and replaced only keeping the best individual and adding $M - 1$ randomly initialised individuals, also resetting δ to $\frac{|P|}{4}$ (cataclysmic mutation).

The number of individuals in the population M was set to 40, ten times the number of filters, and the number of generations was set to 500. To analyse the convergence capability of GAs for filter selection, a hundred iterations of CHC were performed, selecting, from each one of them, the best individual from the last generation.

Additionally, a brute force procedure was designed to test a large number of filter combinations and to select one with the highest performance. In the case of parametric filters, these combinations were generated from constraining the three filter parameters into fixed values. Specifically, CW_N were constrained to take 16 equidistant values between 390 and 890 nm; BW_N, two different values: 64 and 186 nm; and T_N took the three values “bandpass”, “longpass” and “shortpass”. The bandwidth values were selected according to available options that can be commonly found in commercial filters, while the 16 values for the central wavelengths were picked in a constant basis to cover most of the spectral range of interest and to avoid missing wavelengths within it. All these possible values ($16 \times 2 \times 3$) made up a total of 96 different filters to be used. From these, all four filter combinations with repetitions were tested, resulting in $\left(\!\binom{n}{k}\!\right) = \binom{n+k-1}{k} = 3,764,376$ tests, for $n = 96$ and $k = 4$. In the case of COTS filters, as the pool contained 96 models, a brute force approach was also carried out, resulting in a similar number of tests performed.

All data processing was coded using multi-threading in Python 2.7.12, in an Intel® Core™i7-6700 CPU (8 cores, 3.40 GHz) with 32 GB of RAM. For parametric filters, the 100 GA runs took approximately 13.3 hours to complete, and the brute force evaluation lasted for 22.3 hours. For COTS filters, the 100 GA runs took 8.3 hours, while the brute force methodology took 18.5 hours.

3. Results

3.1. Mango spectra

Fig. 5 displays the reflectance plots of the 156 mango spectra used in the simulations. Reflectance values ranged from slightly higher than zero and over 0.8. The spectral profiles have certain similarities with those from other vegetative measurements, like leaves or fruit. These similarities are larger from the characteristic reflectance jump around 700 nm to NIR wavelengths. Most spectrum variations can be found between 500 and 680 nm, a range corresponding to colours that can be present in mango skin at different maturity stages.

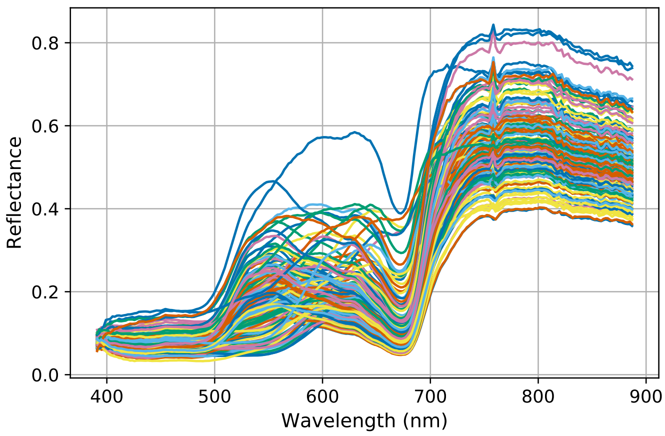

Figure 5: Reflectance plot of the 156 mango spectra acquired under field conditions with a hyperspectral camera from and unmanned ground vehicle. Each spectrum came from averaging all the pixels (spectra) corresponding to each sample (mango).

3.2. RGB and monochrome sensors

To test the accuracy in the extraction of the RGB information from all the samples for the hyperspectral camera, the correlation between this and Prosilica RGB imaging was computed, using the hue channel from HSV space, as shown in Fig. 6. A high correlation was observed with an R^2 score of 0.89. Mango DM prediction models were developed using the three-dimensional RGB input from both imagers, returning R^2 values of 0.55 from RGB_{HSI} and 0.63 from $RGB_{\text{RGB-Camera}}$.

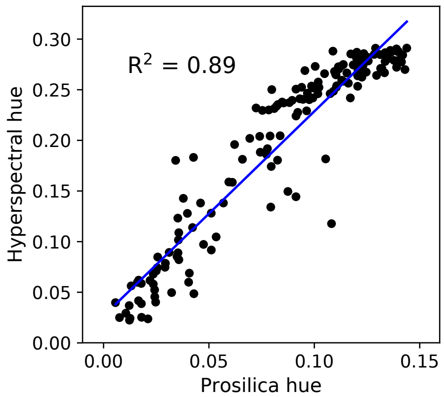

Figure 6: Correlations between the Prosilica RGB camera ($RGB_{\text{RGB-Camera}}$) and hyperspectral data (RGB_{HSI}) for hue after converting to HSV. HSV values were converted from RGB data provided by the Prosilica GT3300 images and after applying the RGB filters in Fig. 4 to hyperspectral data. Each dot represent colour information from the same mango sample.

The results from the brute force approach on the monochrome sensor are presented in Table 1 (column "Monochrome sensor"). The performance values were, in the vast majority of cases, below the 0.2 mark of R^2 (93 out of 96 filters). Only bandpass filters around the 660 nm wavelength revealed a better response for DM estimation, with a peak of 0.40 at BP660 and two shoulders of 0.27 around it, at BP635 and BP695.

The results from the simulation of a RGB sensor with one filter are shown in Table 1 (column "RGB sensor"). The overall trend was much higher than using a monochrome sensor. Half of the filters yielded R^2 scores above 0.50, and three of them (BP550, SP700 and SP701) reached 0.61, very similar to the performance of unfiltered $RGB_{\text{RGB-Camera}}$. It is noteworthy that the $RGB_{\text{RGB-Camera}}$ result previously exposed (R^2 of 0.63), obtained with a SP700 filter mounted in front of the RGB camera, agrees with the simulation of RGB_{HSI} with the same filter (Table 1, column "RGB sensor"), that resulted in an R^2 of 0.61.

3.3. Four monochrome sensors

Results for the selection of four filters in the simulation of a device with four monochrome sensors and four filters are presented in this section. Results are divided into the selection of the best four parametric filters and the best COTS filters. When analysing all the R^2 values reported here, the 0.74 outcome from the DM estimation using the whole HSI spectrum [48] should be taken into consideration as the theoretical maximum performing baseline.

3.3.1. Parametric filter selection

From the 100 GA runs for the selection of parametric filters, the best individual (set of four filters) from the last generation was picked and considered to be the best solution. The average R^2 of these 100 individuals was 0.68, with a standard variation $\sigma = 0.004$ that showed a high level of convergence from all the GA runs. Histograms are shown for the 100 GA solutions central wavelength (Fig. 7), bandwidth (Fig. 8) and type of filter (Fig. 9). For the purpose of creating the histograms, for each individual the four filters were sorted by their central wavelength. Therefore, the first filter was the one with the leftmost central wavelength (lower nm values), while the fourth filter was the one with the higher central wavelengths values.

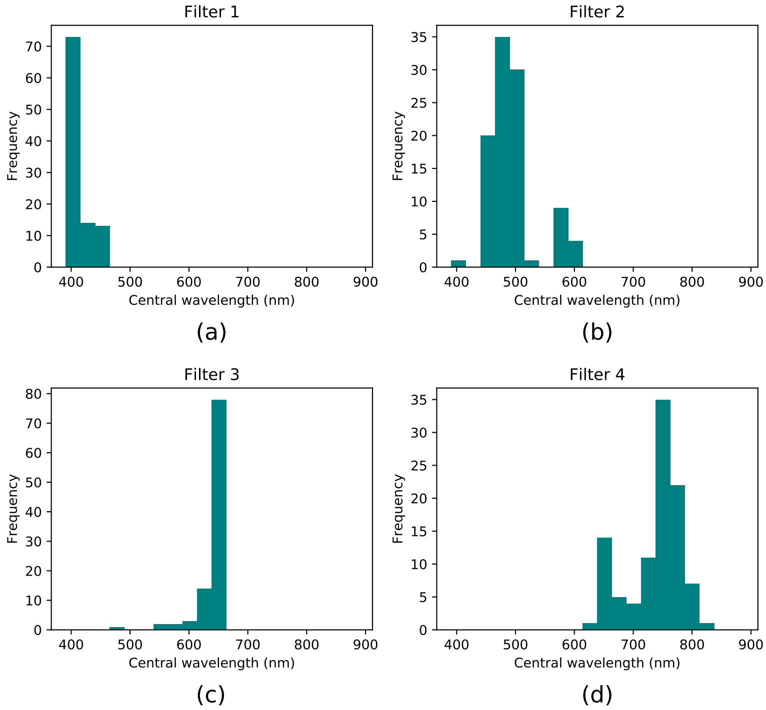

Figure 7: Histograms of the central wavelength of the best individuals from the optimisation with 100 genetic algorithm (GA) runs. Each individual corresponds to the best one from one GA optimisation, and comprises 4 different filters, from number 1 (a), to number 4 (d). For each individual, the four filters were sorted by their central wavelength. Therefore, (a) presents the filters with the leftmost central wavelength (lower nm values), while (d) contains the filters with the higher central wavelengths values.

The general trend shows that, for each parameter, all the filters had a clear convergence peak. This is specially clear for central wavelength, filter 1 (Fig. 7a) centred at 400 nm and filter 3 (Fig. 7c) centred at 650 nm; and for type of filter (Fig. 9), in which there was a strong preference toward bandpass for all the filters. More dispersion was found in the bandwidth histograms (Fig. 8), but still clear convergences towards narrow bandwidths were present in all cases.

From the brute force approach for parametric filter selection, the best result yielded a R^2 of 0.68, slightly lower than the best one of all the 100 GA runs (R^2 of 0.69). Fig. 10 shows the transmission data of the parametric filters selected by both method. In both cases, the central wavelengths of the four filters were extremely similar, but slightly narrower in the case of the GA optimisation (Fig. 10a). The third filter, a bandpass centred around 630 nm, was virtually the same exact one in both approaches, but the high similarity among all four filters highlights the importance of this spectral region.

3.3.2. Commercial filter selection

The average R^2 score from the 100 GA runs in the COTS filter selection was 0.66 ($\sigma < 0.001$). After alphabetically sorting the four filters of each individual, the histograms for the selected filters are shown in Fig. 11. A perfect convergence to filters AB555 and BP635 were achieved by all GA runs (Figs. 11a and b), and filters NF550 and SP510 were selected 97 out of 100 times in Figs. 11c and d.

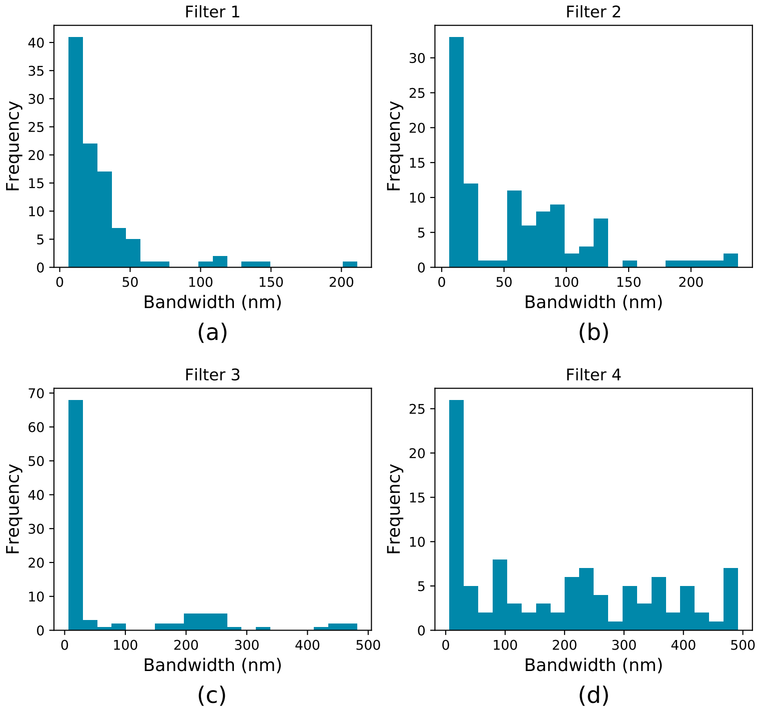

Figure 8: Histograms of the bandwidth of the filters presented in Fig. 7.

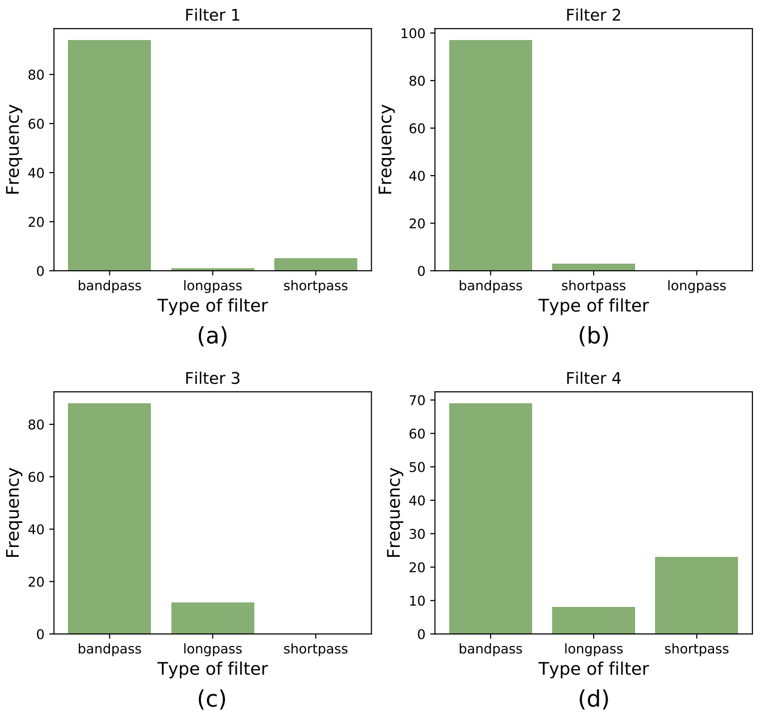

Figure 9: Histogram of the type of the filters presented in Figs. 7.

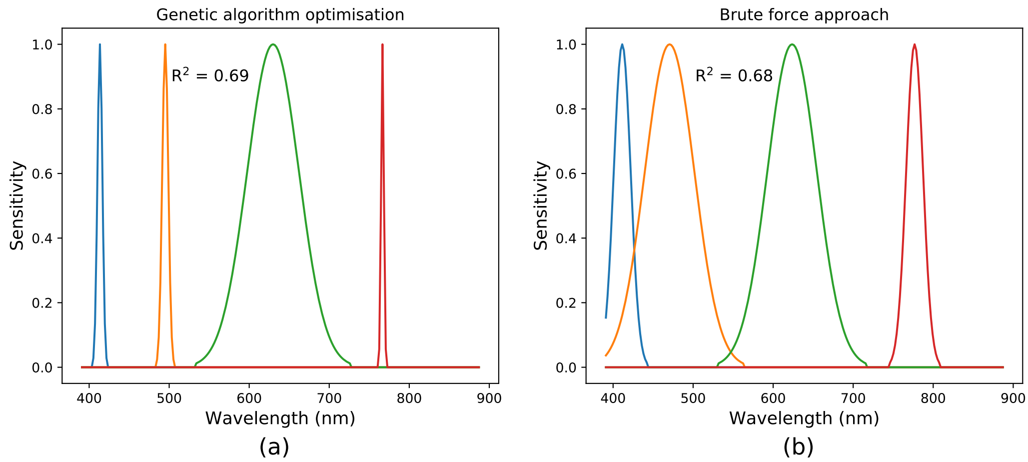

Figure 10: Four parametric filters selected from the best individual from all the 100 genetic algorithm runs (a) and from the brute force approach (b). The R^2 displayed represent the performance of the mango dry matter estimation models after applying the filters to the hyperspectral data.

Fig. 12 shows all the filters selected by the 100 GA runs. In all cases, as also seen in the parametric filter selection (Section 3.3.1), the optimisation highly focused on wavelengths around 600-650 nm and at the beginning of the spectral range. The brute force approach, in which all possible COTS filter combinations with repetitions were tested, selected AB555, BP635, NF550 and SP510 as the best filter combination, with an R^2 of 0.66.

4. Discussion

This paper presented a new methodology for the selection of spectral filters for the estimation of ripeness in mangoes from in-field spectral acquisitions. While HSI for mango dry matter estimation was already demonstrated to be effective under the same conditions in [48], with a baseline R^2 of 0.74, the performance obtained from the multi-spectral sensor simulation in the present study was not far below, with R^2 scores up to 0.68. Both results can be directly compared side-by-side, because the input data were identical, and a similar validation process was used, with five iterations of 5-fold CV to compute the performance statistics. This provides evidence that for the task of mango ripeness estimation, a high level of dimensionality reduction can be performed to spectra within the range from 400 to 900 nm without greatly jeopardising the effectiveness of the machine learning models, although a small performance reduction from the complete HSI data was observed.

The results obtained from the simulation of a monochrome device with a single filter exhibited poor performance for all the filters tested (Table 1, R^2 below 0.10 in the majority of the cases), dissuading the consideration of this solution for DM prediction in mangoes. Yet still, it is worth paying special attention to those bandpass filters around the 660 nm wavelength (BP635, BP660 and BP695), for which the scores, although not good, were clearly higher than the remaining ones. Nevertheless, if a single device is the desired set-up, the best option would be to use a standard RGB camera, as suggested by the results from

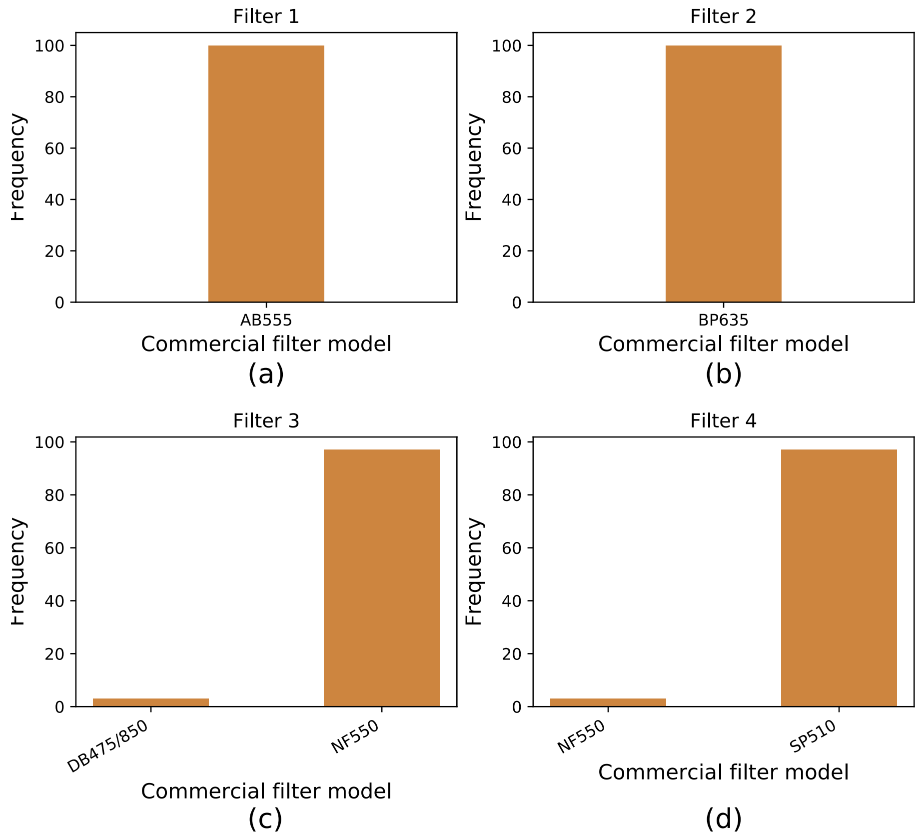

Figure 11: Histogram of the determination coefficient (R^2) of the filter names from the best individuals obtained in the commercial filter optimisation with 100 genetic algorithm runs.

the simulation of a filtered RGB sensor in Table 1 (R^2 up to 0.61 with an SP700) and the actual validation using a real RGB camera with that filter (R^2 of 0.63). This similarity also demonstrated the correctness of the simulations when compared to the real sensor. It is no surprise that RGB imaging alone can be enough to get an acceptable prediction performance, as colour in mangoes is a good indicator of maturity for visual inspection. In the case of the mango DM estimation problem addressed, depending on the level of accuracy sought, RGB alone (with a NIR cut filter) could be considered as an alternative good enough for maturity estimation.

Filters around that spectral region were repeatedly selected when optimising for the four-sensor device. The filter selection performed from the parametric filter pool resulted in a high convergence toward the 640 nm wavelength (Fig. 7c), while the filter BP635 was unanimously selected when optimising from the COTS filter pool (Fig. 11b). This implies that this region is crucial for the prediction of DM in mangoes, and if the development of multi-spectral camera is sought, the inclusion of a bandpass filter centred at approximately 640 nm is critical. The parametric filter selection also had very strong preferences toward lower wavelengths on or around 400 nm and 480 nm (Figs. 7a and b), and this, along with the preference for small bandwidth filters (Figs. 8 and 9), increased the importance of those narrow bands

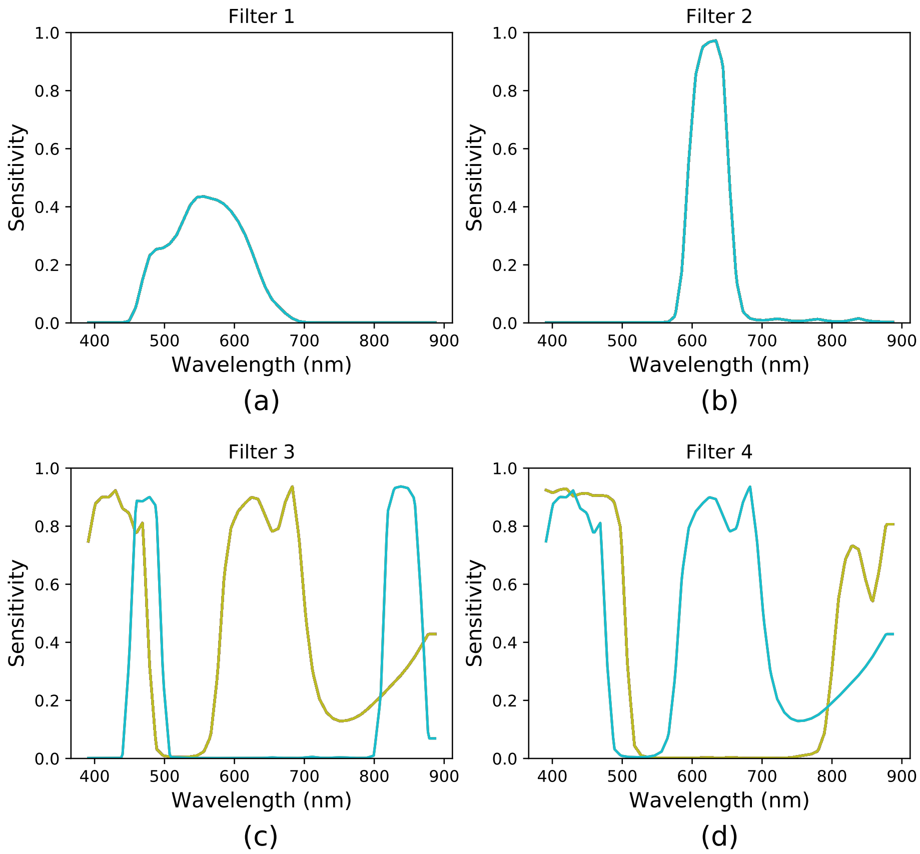

Figure 12: Transmission data of the filters from the best individuals obtained in the commercial filter optimisation with 100 genetic algorithm runs.

in the electromagnetic spectrum. Seemingly, the COTS filter pool offered more limited options, and the optimal solution from the optimisation using that pool would presumably respond worse than a filter selection from parametric tuning. Nevertheless, as observed in the results in Section 3.3.2, the average performance obtained from the COTS filter optimisation (R^2 of 0.66) was very similar than that from the parametric filter optimisation (R^2 of 0.68), showing that for this application, there is no great potential advantage to designing custom bespoke filters, beyond what is already available off the shelf. Similarly to the filter selected in the simulation of a monochrome device, discussed above, both the parametric and commercial solutions also gave strong importance to the same spectral regions, around 650 nm and 400-500 nm (Fig. 12). The identification of the transmittance shapes of several spectral filters (*i.e.*, parametric filter selection) do indeed allow to obtain very fine (virtually, the best) solution for this application. Notwithstanding, in the majority of the cases, these filters are based on theoretical transmittance data (typically from Gaussian curves) with limited practical implementations [22], hence the selection of optimal COTS filters can be considered as a more practical alternative. As demonstrated by the correlation between actual RGB_{HSI} and $RGB_{RGB\text{-}Camera}$ (Fig. 6), the filter simulation in this paper can be assumed to be accurate enough for the filters selected in the simulation of different spectral devices.

The design of the optimisation processes presented in this study has demonstrated suitability for this task, as the best solutions were obtained in virtually all cases. The preference for running a hundred iterations was chosen for the analysis of the convergence capability of GAs, to see if they indeed converge to a global maximum, or get stuck in a local one. In the case of the parametric filter selection (Section 3.3.1), this convergence was almost perfect in terms of the average fitness result obtained in the last generation of each GA run. An R^2 of 0.68 was obtained in virtually all runs, supported by the low standard deviation of these results ($\sigma = 0.004$), meaning that a global maximum was reached. Nevertheless, very similar fitness values were obtained from slightly different values for the optimised parameters. For example, considering the fourth filter, values for central wavelength (Fig. 7d) where not completely focused in narrow ranges, and the same occurred for bandwidth (Fig. 8d), in which, although low bandwidths were preferred, many other values were also picked at some iterations. These different solution options show that several parameter configurations are valid and could lead to optimal performance. Still, the analysis of the parameter histograms from the 100 optimisation runs helps to see the tendency of GAs toward specific values (the most common ones), and thus to focus on those when translating the results to practical implementations. The optimisation using the COTS filter pool converged even more tightly, as the average R^2 value of 0.66 was accompanied by extremely low standard deviation, below 0.001. The best solution was almost unanimously selected (filter models AB555, BP635, NF550 and SP510), making this a clear option for consideration. In summary, all these results bolster that the choice of GA optimisation is a reliable option for spectral filter selection.

The suitability of GAs to solve the objective presented in this paper is not only supported by the analysis of their performance, but also by comparing the outcomes with naive, brute force results. A true, complete brute force approach for parametric filter selection was impossible to carry out. The parameters CW_N and BW_N could potentially take any wavelength value between 400 and 900 nm that, coded as integers, lead to 244 different values for each one of them (the 244 spectral datapoints that represent the hyperspectral camera's spectral range), while T_N can take three different values. Considering that four filters need to be optimised, the total number of combinations is intractably large. For this reason, a subset of these combinations that covers all the ranges had to be used. This explains why the best solution from this brute force approach (Fig. 10b) was slightly lower than the best solution from the 100 optimisation runs (Fig. 10a), R^2 of 0.68 vs. 0.69. Still, the solutions lied within the same central wavelengths, bandwidths and bandpass filter types, as illustrated in Fig. 10, raising GAs as a completely capable alternative for the optimal selection of filters in a reduced fraction of time. The limited number of options in the COTS filter tools made the full brute force approach feasible, testing more than three and a half millions of combinations. The best solution from these was exactly the same one selected in the vast majority of the 100 GA runs (Fig. 11), therefore a single optimisation run would likely select the best solution for COTS filter selection, similarly to a brute force approach, but in less than 20 minutes vs. more than 18 hours. Whether for parametric or COTS filter selection, brute force approaches selected four filters from relatively small pools, and this made it possible to test all the combinations within reasonable times (less than 24 hours of computing, each filter set evaluation taking 0.02 seconds). If, instead of 96, the filter pool would have been doubled, almost two full weeks of computation would have been necessary to test all the valid combinations with brute force. Furthermore, if the same 96 filter pool is maintained, but five filter combinations are tested, the total number of $\left(\binom{96}{5}\right) = 71,523,144$ would have taken 16 days to complete. Optimisation, as opposed to brute force calculation, regardless of the metaheuristic selected, becomes then mandatory for filter selection, and this study demonstrated that GAs provides a stable choice for the optimisation methodology.

The methodology described in this paper could be used as a guideline for a spectral filter design procedure, in a stage previous to hardware selection and assembling. The described pipeline should be adapted in those steps that depend on the specific nature of the problem to solve. For example, the training of prediction models needs to be analysed and defined (considering different strategies, algorithms, validation procedures, etc.); other different kinds of spectral filters may be simulated, having new parameters to optimise; or even the total number of sensors may vary (*e.g.*, optical devices with 3 or 5 sensors and filters). The results from the simulations could therefore be aggregated to a hardware selection step, considering the current alternatives and their cost vs. the potential cost and performance of the simulated devices.

5. Conclusions

This paper presented a new alternative for the selection of spectral filters to estimate mango ripeness from hyperspectral imaging acquired in-field from an unmanned ground vehicle. The selection was carried out not by specific band picking, as commonly described in the HSI literature, but simulating several multi-spectral sensors with filters having different transmittance responses, using parametric and commercial filter pools. The simulations and analyses of several different devices demonstrated that, by converting the goal into an optimisation problem, genetic algorithms were able to obtain the best solution for dry matter prediction more efficiently than using brute force approaches. While HSI was already demonstrated to be adequate for ripeness estimation in mangoes, the results in this paper show that dimensionality reduction is feasible while still maintaining an acceptable performance of the prediction models. This allows future work towards building lower cost devices that are customised towards monitoring specific traits with relevance to precision agriculture, and for mango dry matter specifically.

Acknowledgements

Salvador Gutiérrez would like to acknowledge the research funding FPI grant 299/2016 by Universidad de La Rioja, Gobierno de La Rioja. This work is supported by the Australian Centre for Field Robotics (ACFR) at The University of Sydney. Thanks to Simpson Farms and Chad Simpson for their support and to Nicholas Anderson and Kerry Walsh for providing the ground truth dry matter measurements.

References

[1] Allied Vision Technologies GmbH. Prosilica GT3300 specifications. `https://www.alliedvision.com/en/products/cameras/detail/Prosilica%20GT/3300.html`. Accessed: 2018-11-21.

[2] Anderson, N. T., Subedi, P. P., and Walsh, K. B. Manipulation of mango fruit dry matter content to improve eating quality. *Scientia Horticulturae 226* (2017), 316–321.

[3] Bodner, G., Nakhforoosh, A., Arnold, T., and Leitner, D. Hyperspectral imaging: a novel approach for plant root phenotyping. *Plant methods 14*, 1 (2018), 84.

[4] Chang, Y.-L., Liu, J.-N., Chen, Y.-L., Chang, W.-Y., Hsieh, T.-J., and Huang, B. Hyperspectral band selection based on parallel particle swarm optimization and impurity function band prioritization schemes. *Journal of Applied Remote Sensing 8*, 1 (2014), 084798.

[5] Deery, D., Jimenez-Berni, J., Jones, H., Sirault, X., and Furbank, R. Proximal remote sensing buggies and potential applications for field-based phenotyping. *Agronomy 4*, 3 (2014), 349–379.

[6] Diago, M. P., Fernández-Novales, J., Fernandes, A. M., Melo-Pinto, P., and Tardaguila, J. Use of visible and short-wave near-infrared hyperspectral imaging to fingerprint anthocyanins in intact grape berries. *Journal of agricultural and food chemistry 64*, 40 (2016), 7658–7666.

[7] dos Santos Neto, J. P., de Assis, M. W. D., Casagrande, I. P., Júnior, L. C. C., and de Almeida Teixeira, G. H. Determination of 'Palmer' mango maturity indices using portable near infrared (VIS-NIR) spectrometer. *Postharvest Biology and Technology 130* (2017), 75–80.

[8] Drew, M. S., and Finlayson, G. D. Analytic solution for separating spectra into illumination and surface reflectance components. *JOSA A 24*, 2 (2007), 294–303.

[9] Eshelman, L. J. The chc adaptive search algorithm: How to have safe search when engaging in nontraditional genetic recombination. In *Foundations of genetic algorithms*, vol. 1. Elsevier, 1991, pp. 265–283.

[10] Felix Instruments, Inc. Mango data collection standard operating procedure. `https://felixinstruments.com/static/media/uploads/mango_data-collection_sop.pdf`. Accessed: 2019-05-30.

[11] Fernandes, A. M., Melo-Pinto, P., Millan, B., Tardáguila, J., and Diago, M. P. Automatic discrimination of grapevine (vitis vinifera l.) clones using leaf hyperspectral imaging and partial least squares. *The Journal of Agricultural Science 153*, 3 (2015), 455–465.

[12] Ganesan, V. S. K., and Vasuki, S. Maximin distance based band selection for endmember extraction in hyperspectral images using simplex growing algorithm. *Multimedia Tools and Applications 77*, 6 (2018), 7221–7237.

[13] Gao, J., Du, Q., Gao, L., Sun, X., and Zhang, B. Ant colony optimization-based supervised and unsupervised band selections for hyperspectral urban data classification. *Journal of Applied Remote Sensing 8*, 1 (2014), 085094.

[14] Giovenzana, V., Beghi, R., Parisi, S., Brancadoro, L., and Guidetti, R. Potential effectiveness of visible and near infrared spectroscopy coupled with wavelength selection for real time grapevine leaf water status measurement. *Journal of the Science of Food and Agriculture 98*, 5 (2018), 1935–1943.

[15] Gutiérrez, S., Fernández-Novales, J., Diago, M. P., and Tardaguila, J. On-the-go hyperspectral imaging under field conditions and machine learning for the classification of grapevine varieties. *Frontiers in plant science 9* (2018).

[16] Gutiérrez, S., Wendel, A., and Underwood, J. Ground based hyperspectral imaging for extensive mango yield estimation. *Computers and Electronics in Agriculture 157* (2019), 126–135.

[17] Haneishi, H., Hasegawa, T., Hosoi, A., Yokoyama, Y., Tsumura, N., and Miyake, Y. System design for accurately estimating the spectral reflectance of art paintings. *Applied Optics 39*, 35 (2000), 6621–6632.

[18] Hardeberg, J. Y. Filter selection for multispectral color image acquisition. *Journal of Imaging Science and Technology 48*, 2 (2004), 105–110.

[19] Huang, L., Zhou, Y., Meng, L., Wu, D., and He, Y. Comparison of different ccd detectors and chemometrics for predicting total anthocyanin content and antioxidant activity of mulberry fruit using visible and near infrared hyperspectral imaging technique. *Food chemistry 224* (2017), 1–10.

[20] Huang, P., Luo, X., Jin, J., Wang, L., Zhang, L., Liu, J., and Zhang, Z. Improving high-throughput phenotyping using fusion of close-range hyperspectral camera and low-cost depth sensor. *Sensors 18*, 8 (2018), 2711.

[21] Imai, F. H., Quan, S., Rosen, M. R., and Berns, R. S. Digital camera filter design for colorimetric and spectral accuracy. In *Proc. of third international conference on multispectral color science* (2001), University of Joensuu, Finland, pp. 13–16.

[22] Lapray, P.-J., Wang, X., Thomas, J.-B., and Gouton, P. Multispectral filter arrays: Recent advances and practical implementation. *Sensors 14*, 11 (2014), 21626–21659.

[23] Li, S., Qiu, J., Yang, X., Liu, H., Wan, D., and Zhu, Y. A novel approach to hyperspectral band selection based on spectral shape similarity analysis and fast branch and bound search. *Engineering Applications of Artificial Intelligence 27* (2014), 241–250.

[24] Li, X., Wei, Y., Xu, J., Feng, X., Wu, F., Zhou, R., Jin, J., Xu, K., Yu, X., and He, Y. Ssc and ph for sweet assessment and maturity classification of harvested cherry fruit based on nir hyperspectral imaging technology. *Postharvest Biology and Technology 143* (2018), 112–118.

[25] Li, Y., Majumder, A., Zhang, H., and Gopi, M. Optimized multi-spectral filter array based imaging of natural scenes. *Sensors 18*, 4 (2018), 1172.

[26] Liu, Z.-Y., Qi, J.-G., Wang, N.-N., Zhu, Z.-R., Luo, J., Liu, L.-J., Tang, J., and Cheng, J.-A. Hyperspectral dis-

crimination of foliar biotic damages in rice using principal component analysis and probabilistic neural network. *Precision Agriculture* (2018), 1–19.

[27] Midwest Optical Systems, Inc. MIDOPT commercial filter specifications used in this study. `http://midopt.com/filters/`. Accessed: 2018-11-21.

[28] Moghimi, A., Yang, C., Miller, M. E., Kianian, S. F., and Marchetto, P. M. A novel approach to assess salt stress tolerance in wheat using hyperspectral imaging. *Frontiers in plant science 9* (2018).

[29] Morel, J., Jay, S., Féret, J.-B., Bakache, A., Bendoula, R., Carreel, F., and Gorretta, N. Exploring the potential of procosine and close-range hyperspectral imaging to study the effects of fungal diseases on leaf physiology. *Scientific reports 8*, 1 (2018), 15933.

[30] Nagasubramanian, K., Jones, S., Sarkar, S., Singh, A. K., Singh, A., and Ganapathysubramanian, B. Hyperspectral band selection using genetic algorithm and support vector machines for early identification of charcoal rot disease in soybean stems. *Plant methods 14*, 1 (2018), 86.

[31] Park, B., and Lu, R. *Hyperspectral imaging technology in food and agriculture.* Springer, 2015.

[32] Paul, A., Bhattacharya, S., Dutta, D., Sharma, J. R., and Dadhwal, V. K. Band selection in hyperspectral imagery using spatial cluster mean and genetic algorithms. *GIScience & Remote Sensing 52*, 6 (2015), 643–659.

[33] Pedregosa, F., Varoquaux, G., Gramfort, A., Michel, V., Thirion, B., Grisel, O., Blondel, M., Prettenhofer, P., Weiss, R., Dubourg, V., Vanderplas, J., Passos, A., Cournapeau, D., Brucher, M., Perrot, M., and Duchesnay, E. Scikit-learn: Machine learning in Python. *Journal of Machine Learning Research 12* (2011), 2825–2830.

[34] Péguillet, H., Thomas, J.-B., Gouton, P., and Ruichek, Y. Energy balance in single exposure multispectral sensors. In *Colour and Visual Computing Symposium (CVCS), 2013* (2013), IEEE, pp. 1–6.

[35] Rungpichayapichet, P., Nagle, M., Yuwanbun, P., Khuwijitjaru, P., Mahayothee, B., and Müller, J. Prediction mapping of physicochemical properties in mango by hyperspectral imaging. *Biosystems Engineering 159* (2017), 109–120.

[36] Skoog, D. A., Holler, F. J., and Crouch, S. R. *Principles of instrumental analysis.* Cengage learning, 2017.

[37] Stein, M., Bargoti, S., and Underwood, J. Image based mango fruit detection, localisation and yield estimation using multiple view geometry. *Sensors 16*, 11 (2016), 1915.

[38] Sun, D.-W. *Hyperspectral imaging for food quality analysis and control.* Elsevier, 2010.

[39] Sun, X., Yang, L., Shen, Q., Ni, L., and Zhang, B. A new ant colony optimization algorithm based band selection method. In *Hyperspectral Image and Signal Processing: Evolution in Remote Sensing (WHISPERS), 2014 6th Workshop on* (2014), IEEE, pp. 1–4.

[40] Suomalainen, J., Anders, N., Iqbal, S., Roerink, G., Franke, J., Wenting, P., Hünniger, D., Bartholomeus, H., Becker, R., and Kooistra, L. A lightweight hyperspectral mapping system and photogrammetric processing chain for unmanned aerial vehicles. *Remote Sensing 6*, 11 (2014), 11013–11030.

[41] Susič, N., Žibrat, U., Širca, S., Strajnar, P., Razinger, J., Knapič, M., Vončina, A., Urek, G., and Stare, B. G. Discrimination between abiotic and biotic drought stress in tomatoes using hyperspectral imaging. *Sensors and Actuators B: Chemical 273* (2018), 842–852.

[42] Tang, K., Xie, L., and Li, G. A multiple classifier system based on ant-colony optimization for hyperspectral image classification. In *Journal of Physics: Conference Series* (2017), vol. 787, IOP Publishing, p. 012011.

[43] Tian, X., Li, J., Wang, Q., Fan, S., and Huang, W. A bi-layer model for nondestructive prediction of soluble solids content in apple based on reflectance spectra and peel pigments. *Food chemistry 239* (2018), 1055–1063.

[44] Walsh, K., and Subedi, P. In-field monitoring of mango fruit dry matter for maturity estimation. In *XXIX International Horticultural Congress on Horticulture: Sustaining Lives, Livelihoods and Landscapes (IHC2014): 1119* (2014), pp. 273–278.

[45] Wang, X., Thomas, J.-B., Hardeberg, J. Y., and Gouton, P. A study on the impact of spectral characteristics of filters on multispectral image acquisition. In *12th Congress of the International Colour Association* (2013), vol. 4, pp. 1765–1768.

[46] Wendel, A., and Underwood, J. Extrinsic parameter calibration for line scanning cameras on ground vehicles with navigation systems using a calibration pattern. *Sensors 17*, 11 (2017), 2491.

[47] Wendel, A., and Underwood, J. Illumination compensation in ground based hyperspectral imaging. *ISPRS Journal of Photogrammetry and Remote Sensing 129* (2017), 162–178.

[48] Wendel, A., Underwood, J., and Walsh, K. Maturity estimation of mangoes using hyperspectral imaging from a

ground based mobile platform. *Computers and Electronics in Agriculture 155* (2018), 298–313.

[49] Williams, D., Britten, A., McCallum, S., Jones, H., Aitkenhead, M., Karley, A., Loades, K., Prashar, A., and Graham, J. A method for automatic segmentation and splitting of hyperspectral images of raspberry plants collected in field conditions. *Plant methods 13*, 1 (2017), 74.

[50] Xu, M., Shi, J., Chen, W., Shen, J., Gao, H., and Zhao, J. A band selection method for hyperspectral image based on particle swarm optimization algorithm with dynamic sub-swarms. *Journal of Signal Processing Systems* (2018), 1–11.

[51] Yasuma, F., Mitsunaga, T., Iso, D., and Nayar, S. K. Generalized assorted pixel camera: postcapture control of resolution, dynamic range, and spectrum. *IEEE transactions on image processing 19*, 9 (2010), 2241–2253.

[52] Zhang, M., Gong, M., and Chan, Y. Hyperspectral band selection based on multi-objective optimization with high information and low redundancy. *Applied Soft Computing 70* (2018), 604 – 621.

[53] Zhang, M., Ma, J., and Gong, M. Unsupervised hyperspectral band selection by fuzzy clustering with particle swarm optimization. *IEEE Geoscience and Remote Sensing Letters 14*, 5 (2017), 773–777.

[54] Zhang, Q., Li, Q., and Zhang, G. Rapid determination of leaf water content using vis/nir spectroscopy analysis with wavelength selection. *Journal of Spectroscopy 27*, 2 (2012), 93–105.

Table 1: Determination coefficients (R^2) from applying one single commercial off-the-shelf (COTS) filter to raw reflectance spectrum in the range from 400 to 900 nm (Raw spectrum) or to apply one single COTS filter to a reflectance spectrum after applying RGB filters (RGB_{HSI}).

Filter applied	Monochrome sensor	RGB sensor	Filter applied	Monochrome	RGB sensor
AB555	0.00	0.57	LP515	0.03	0.58
AC370	0.03	0.55	LP530	0.04	0.59
AC380	0.03	0.56	LP550	0.05	0.60
AC685	0.01	0.06	LP580	0.06	0.51
AC760	0.00	0.03	LP590	0.06	0.38
AC800	0.00	0.03	LP610	0.06	0.39
AC850	0.00	0.03	LP630	0.05	0.41
AC900	0.00	0.03	LP645	0.04	0.39
BP250	0.02	0.43	LP665	0.02	0.22
BP324	0.13	0.22	LP695	0.00	0.04
BP365	0.00	0.00	LP715	0.00	0.01
BP470	0.00	0.16	LP780	0.00	0.03
BP485	0.01	0.59	LP800	0.00	0.03
BP500	0.00	0.57	LP815	0.00	0.03
BP505	0.05	0.38	LP830	0.00	0.03
BP525	0.06	0.38	LP850	0.00	0.03
BP540	0.06	0.43	LP900	0.00	0.03
BP550	0.07	0.61	LP920	0.01	0.03
BP590	0.00	0.46	ND030	0.03	0.55
BP635	0.27	0.44	ND060	0.03	0.56
BP660	0.40	0.38	ND090	0.03	0.52
BP695	0.27	0.27	ND120	0.03	0.51
BP735	0.02	0.04	ND200	0.01	0.45
BP800	0.00	0.01	ND300	0.01	0.22
BP810	0.00	0.03	ND400	0.01	0.06
BP845	0.00	0.03	NF550	0.15	0.55
BP850	0.00	0.03	Ni030	0.03	0.55
BP865	0.00	0.03	Ni060	0.03	0.55
BP880	0.00	0.03	Ni090	0.03	0.56
DB395/870	0.00	0.00	Ni120	0.03	0.55
DB475/850	0.00	0.00	Ni200	0.02	0.54
DB550/850	0.02	0.26	PE530	0.00	0.57
DB660/850	0.09	0.55	SP510	0.00	0.02
DB735	0.01	0.53	SP570	0.03	0.39
DB850	0.01	0.59	SP585	0.01	0.26
DB940	0.02	0.60	SP625	0.00	0.56
FL550	0.03	0.55	SP635	0.01	0.59
LA080	0.03	0.56	SP644	0.01	0.58
LA120	0.04	0.59	SP645	0.01	0.59
LB080	0.01	0.50	SP650	0.01	0.59
LB120	0.01	0.51	SP675	0.03	0.60
LP285	0.03	0.55	SP700	0.07	0.61
LP330	0.03	0.55	SP701	0.08	0.61
LP340	0.03	0.55	SP705	0.04	0.59
LP390	0.03	0.55	SP730	0.08	0.60
LP415	0.03	0.56	SP785	0.06	0.58
LP470	0.03	0.58	TB475/550/850	0.01	0.27
LP500	0.03	0.58	TB550/660/850	0.01	0.60

R^2 values were obtained from five iterations of 5-fold cross validation using linear regression in the “Raw spectrum” column and support vector machines in “RGB” column. The names of the COTS filter models refer to [27]. As a general rule, the letters BP refer to “bandpass”, LP to “longpass”, SP to “shortpass”, ND and Ni to “neutral density”, LB to “light balancing” and AC to “acrylic”; while the number after the letters refer to the main central wavelength in nm.

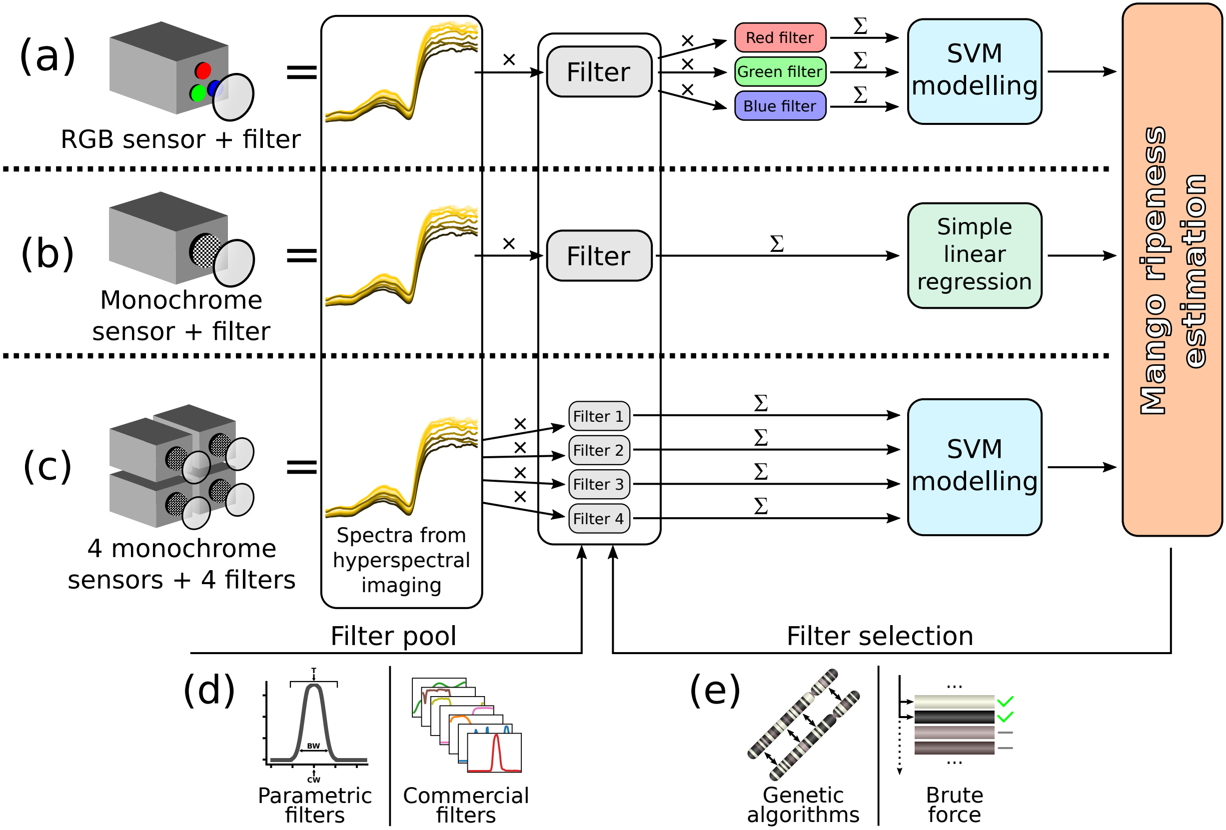
(a)
RGB sensor + filter
(b)
Monochrome sensor + filter
(c)
4 monochrome sensors + 4 filters
Spectra from hyperspectral imaging
Filter
Red filter
Green filter
Blue filter
SVM modelling
Simple linear regression
Filter 1
Filter 2
Filter 3
Filter 4
Mango ripeness estimation
Filter pool
Filter selection
(d)
BW
CW
Parametric filters
Commercial filters
(e)
Genetic algorithms
Brute force

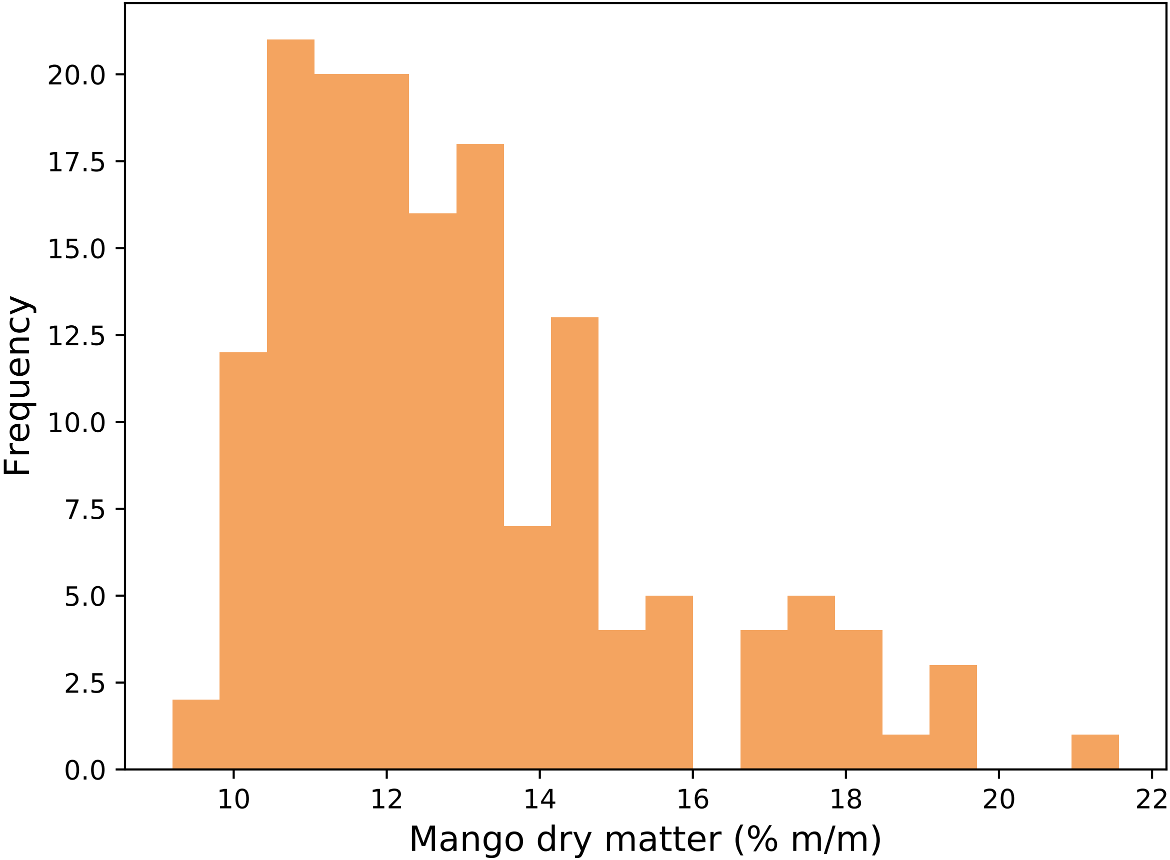

Frequency
20.0
17.5
15.0
12.5
10.0
7.5
5.0
2.5
0.0
10
12
14
16
18
20
22
Mango dry matter (% m/m)


RGB camera
Hyperspectral camera
SICK
SHRIMP
THE UNIVERSITY OF SYDNEY
Horticulture Innovation Australia
Reference panels
Mango trays

(a) (b)

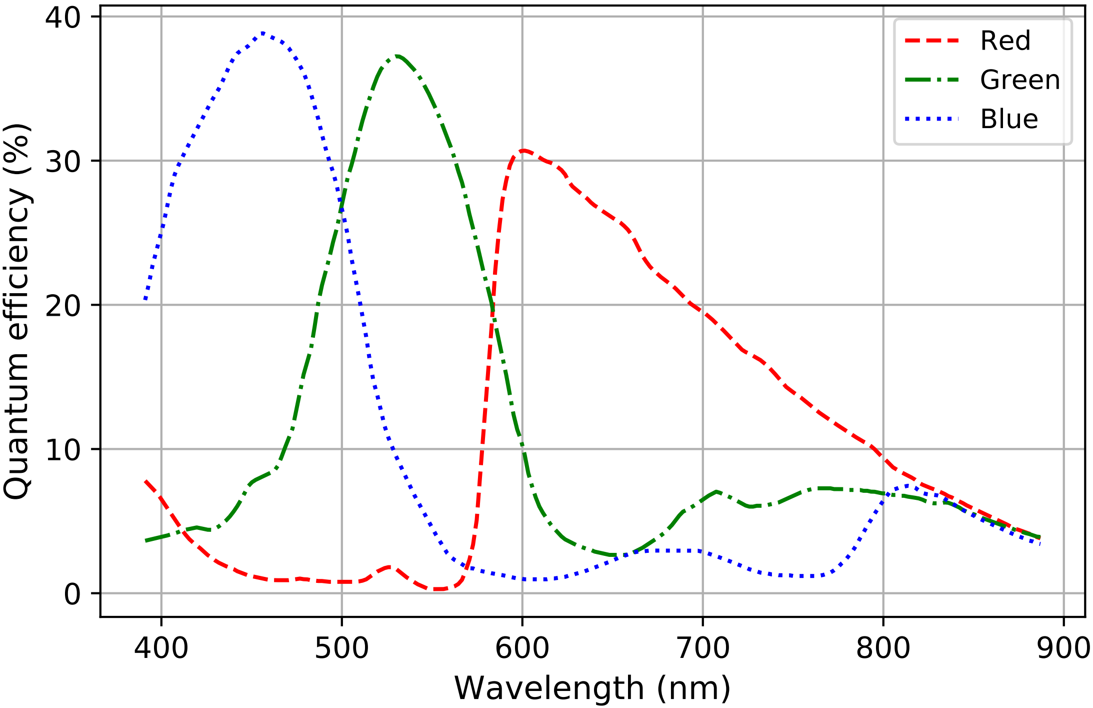
Red
Green
Blue
Quantum efficiency (%)
Wavelength (nm)
0
10
20
30
40
400
500
600
700
800
900

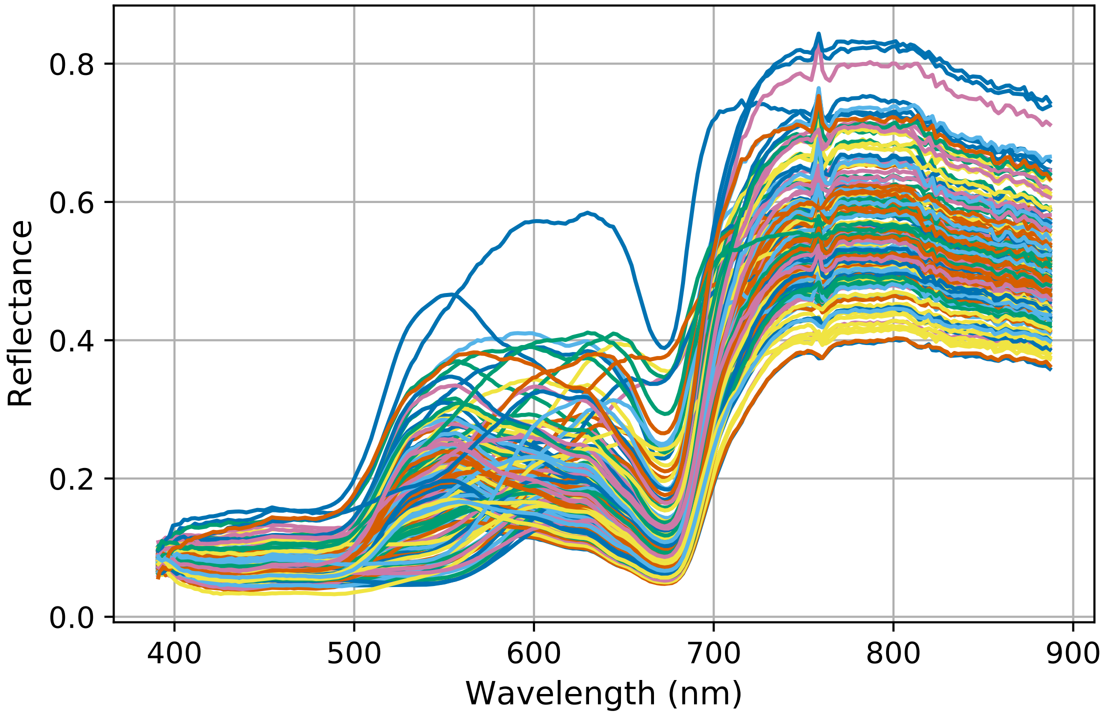
0.8
0.6
0.4
0.2
0.0
Reflectance
400
500
600
700
800
900
Wavelength (nm)

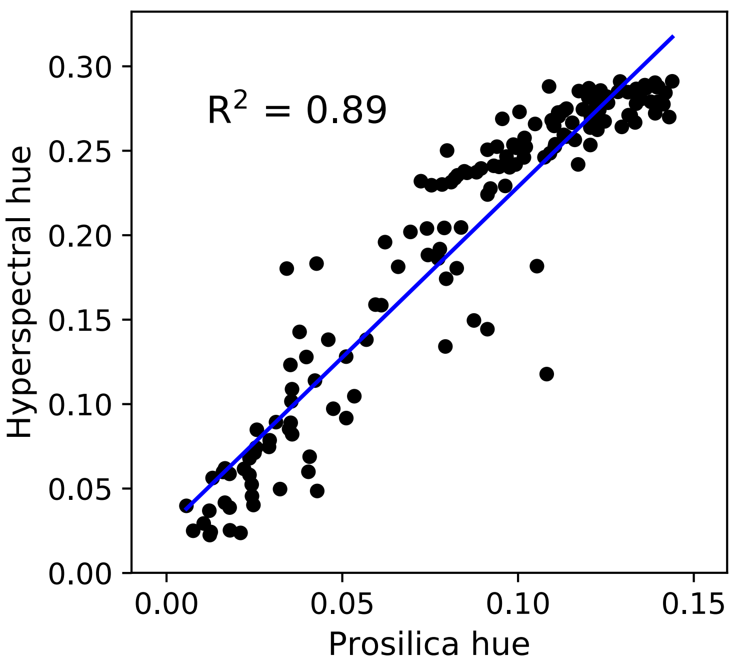
$R^2 = 0.89$
Hyperspectral hue
Prosilica hue
0.00
0.05
0.10
0.15
0.20
0.25
0.30
0.00
0.05
0.10
0.15

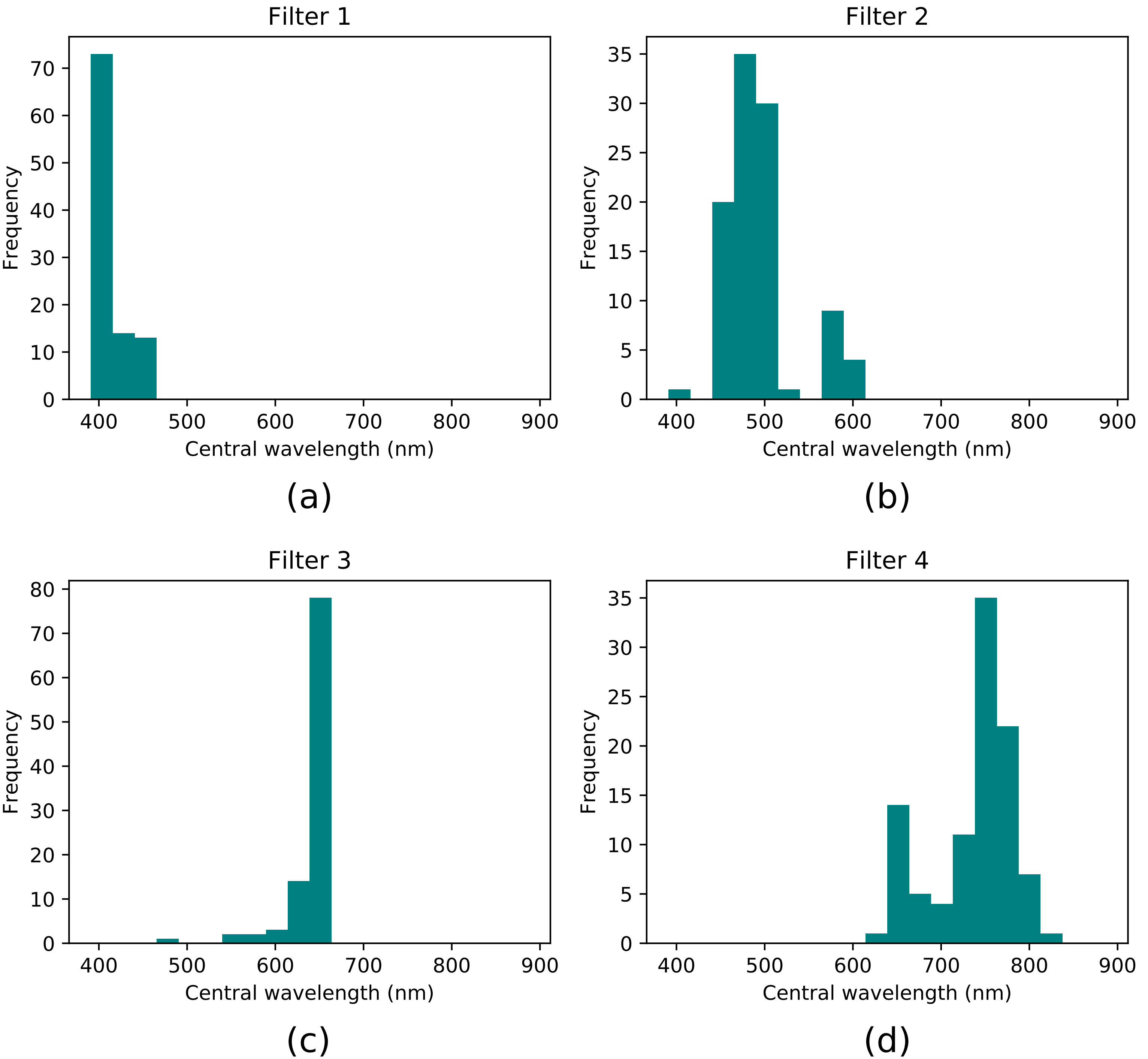
Filter 1
Frequency
0
10
20
30
40
50
60
70
400
500
600
700
800
900
Central wavelength (nm)
(a)
Filter 2
Frequency
0
5
10
15
20
25
30
35
400
500
600
700
800
900
Central wavelength (nm)
(b)
Filter 3
Frequency
0
10
20
30
40
50
60
70
80
400
500
600
700
800
900
Central wavelength (nm)
(c)
Filter 4
Frequency
0
5
10
15
20
25
30
35
400
500
600
700
800
900
Central wavelength (nm)
(d)

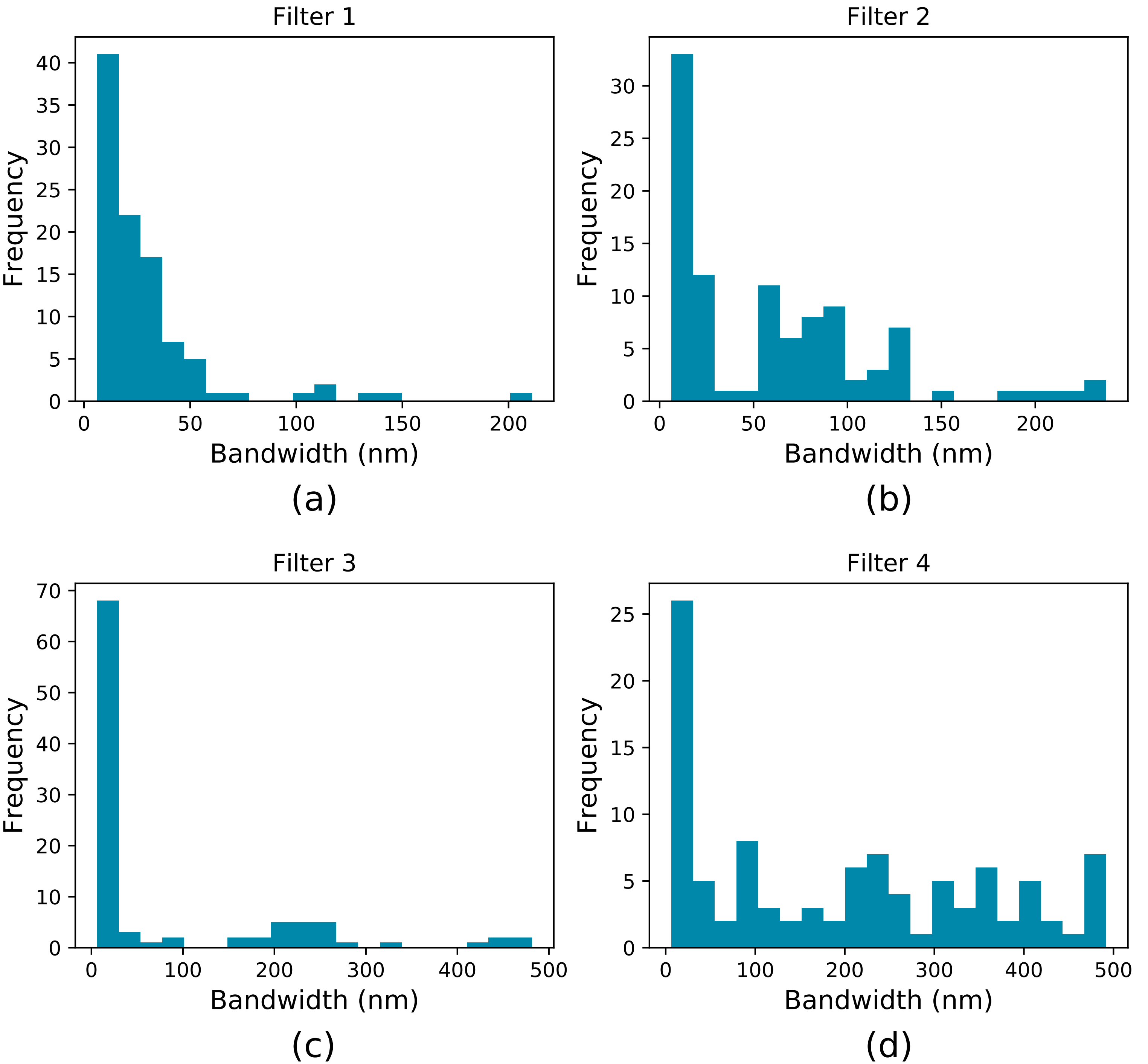
Filter 1
Frequency
Bandwidth (nm)
(a)
Filter 2
Frequency
Bandwidth (nm)
(b)
Filter 3
Frequency
Bandwidth (nm)
(c)
Filter 4
Frequency
Bandwidth (nm)
(d)

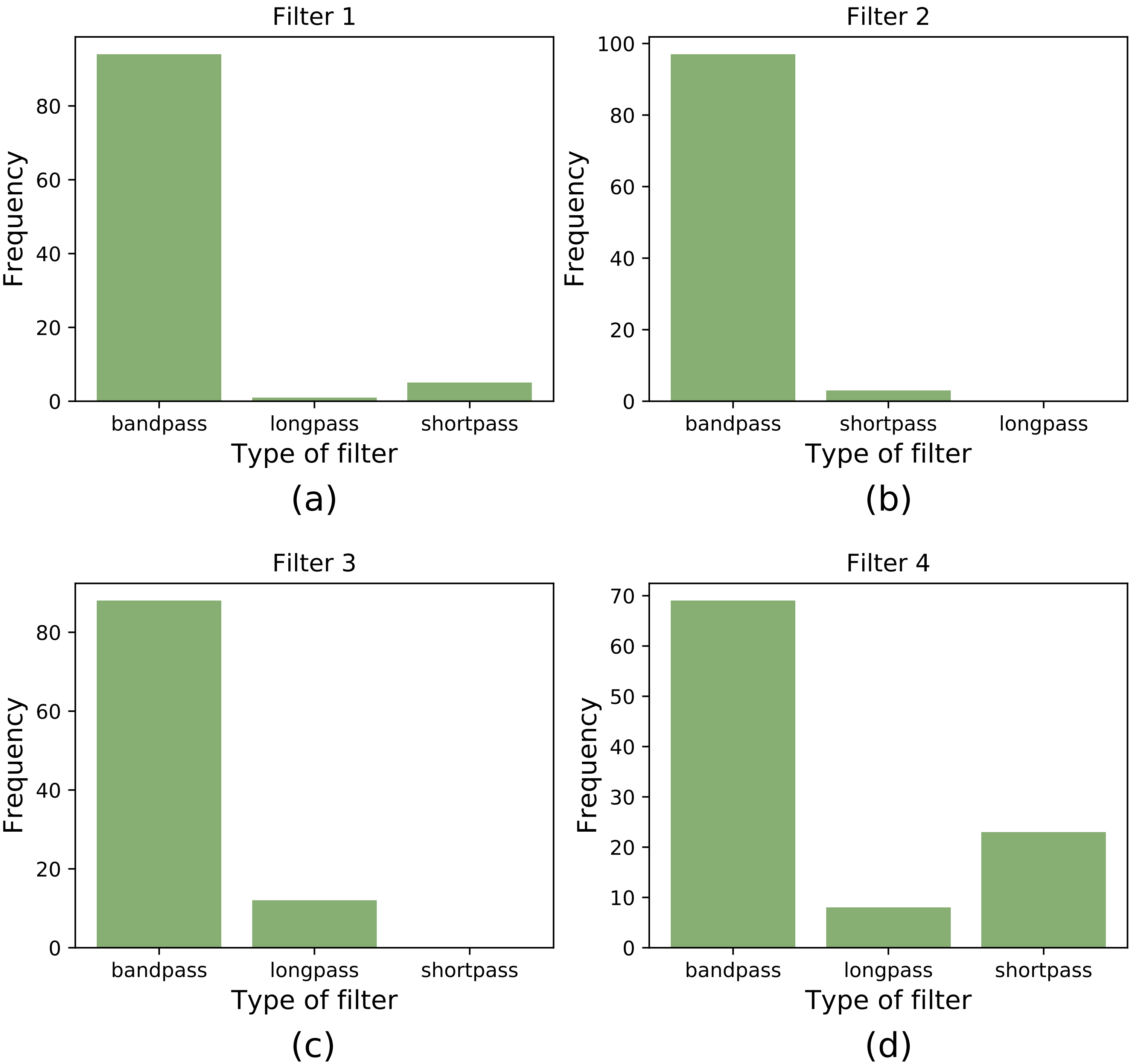
Filter 1
Frequency
0
20
40
60
80
bandpass
longpass
shortpass
Type of filter
(a)
Filter 2
Frequency
0
20
40
60
80
100
bandpass
shortpass
longpass
Type of filter
(b)
Filter 3
Frequency
0
20
40
60
80
bandpass
longpass
shortpass
Type of filter
(c)
Filter 4
Frequency
0
10
20
30
40
50
60
70
bandpass
longpass
shortpass
Type of filter
(d)

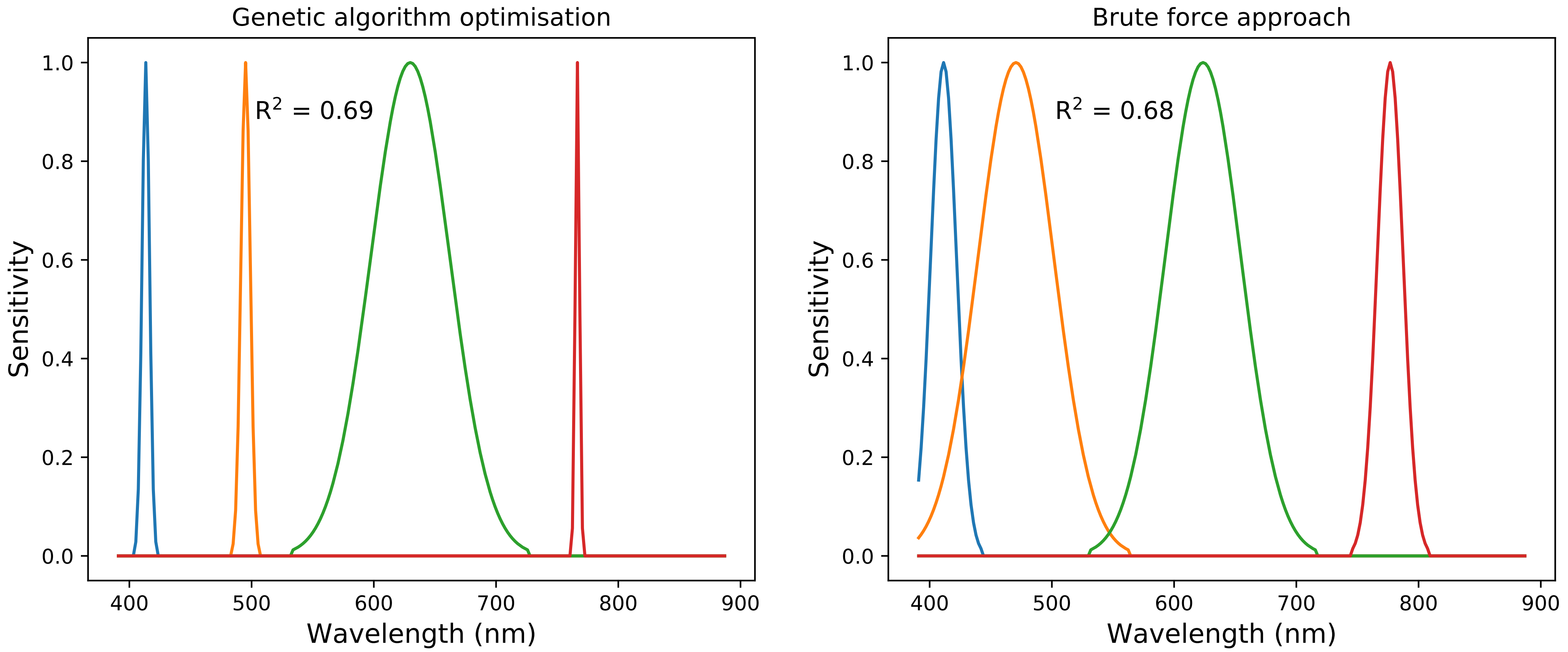
Genetic algorithm optimisation
R^2 = 0.69
Sensitivity
1.0
0.8
0.6
0.4
0.2
0.0
400
500
600
700
800
900
Wavelength (nm)
Brute force approach
R^2 = 0.68
Sensitivity
1.0
0.8
0.6
0.4
0.2
0.0
400
500
600
700
800
900
Wavelength (nm)

(a) (b)

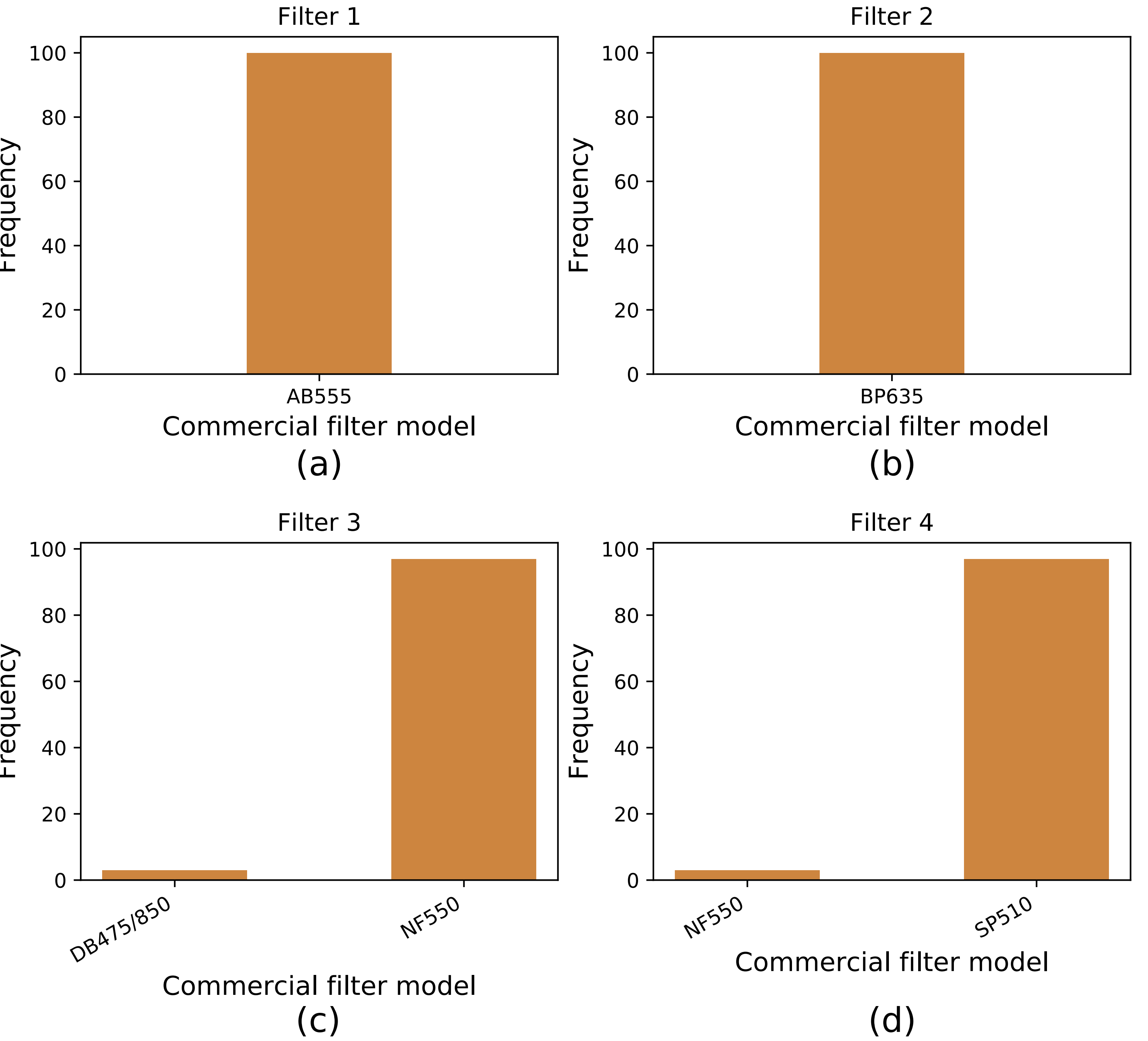

Filter 1
Frequency
100
80
60
40
20
0
AB555
Commercial filter model
(a)
Filter 2
Frequency
100
80
60
40
20
0
BP635
Commercial filter model
(b)
Filter 3
Frequency
100
80
60
40
20
0
DB475/850
NF550
Commercial filter model
(c)
Filter 4
Frequency
100
80
60
40
20
0
NF550
SP510
Commercial filter model
(d)

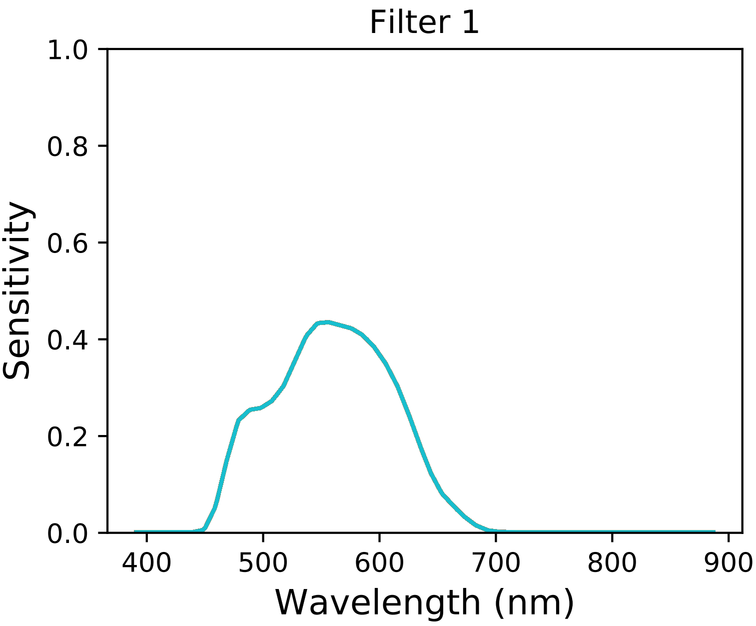
Filter 1
1.0
0.8
0.6
0.4
0.2
0.0
Sensitivity
400
500
600
700
800
900
Wavelength (nm)

(a)

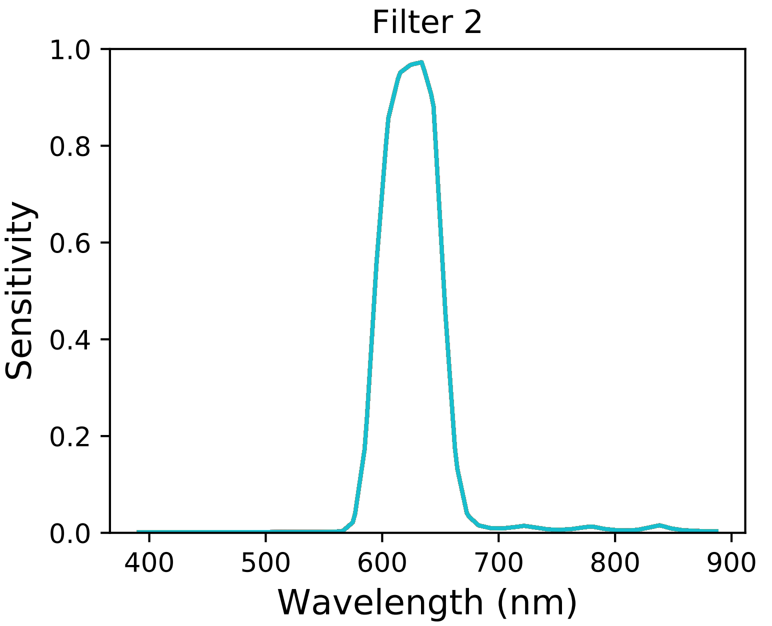
Filter 2
1.0
0.8
0.6
0.4
0.2
0.0
Sensitivity
400
500
600
700
800
900
Wavelength (nm)

(b)

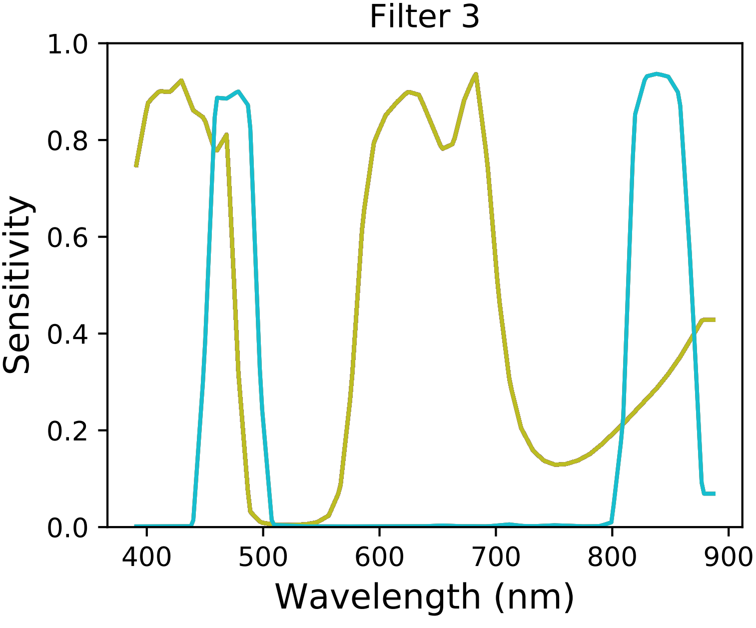
Filter 3
1.0
0.8
0.6
0.4
0.2
0.0
Sensitivity
400
500
600
700
800
900
Wavelength (nm)

(c)

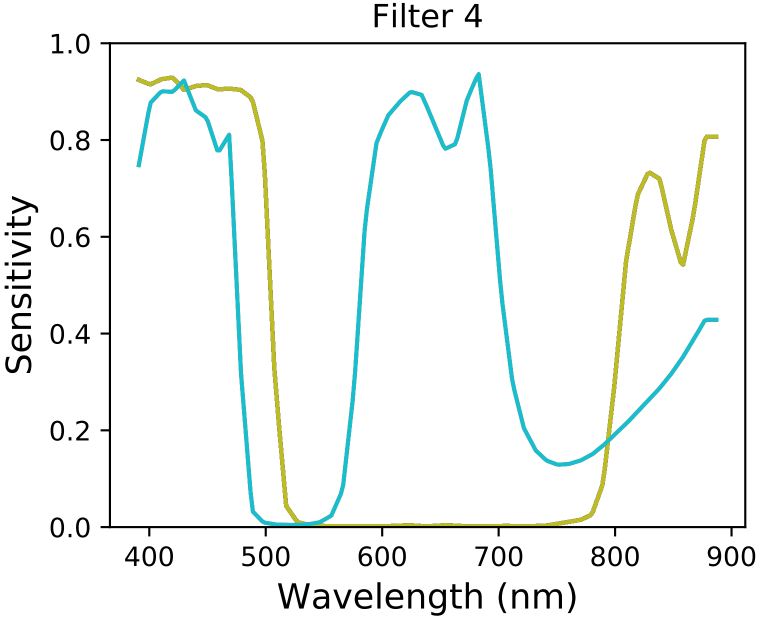
Filter 4
1.0
0.8
0.6
0.4
0.2
0.0
Sensitivity
400
500
600
700
800
900
Wavelength (nm)

(d)

Function f:

$C1, B1, T1, C2, B2, T2, C3, B3, T3, C4, B4, T4 \leftarrow$ input; the values of central wavelength, bandwidth and type of filter of the four filters to be applied to the raw spectra

$X \leftarrow$ an empty set
$y \leftarrow$ the set of dry matter values of all the samples

f1 $\leftarrow$ getFilter($C1, B1, T1$)
f2 $\leftarrow$ getFilter($C2, B2, T2$)
f3 $\leftarrow$ getFilter($C3, B3, T3$)
f4 $\leftarrow$ getFilter($C4, B4, T4$)

for *each spectrum from the raw spectra* **do**
  $x1 \leftarrow$ applyFilter($spectrum, f1$)
  $x2 \leftarrow$ applyFilter($spectrum, f2$)
  $x3 \leftarrow$ applyFilter($spectrum, f3$)
  $x4 \leftarrow$ applyFilter($spectrum, f4$)

  The set $\{x1, x2, x3, x4\}$ is added to X as a new sample
end

scores $\leftarrow$ an empty set

for *each* $i \in \{1, 2, 3, 4, 5\}$ **do**
  regressor $\leftarrow$ an ε-SVM is set up as regressor
  $R^2 \leftarrow$ performCrossValidation($regressor, X, y, folds = 5, seed = i$)
  R^2 is added to *scores*
end

fitness $\leftarrow$ average($scores$)

return *fitness*

Algorithm 1: Implementation of the fitness function *f*. The function "getFilters" receives three values for central wavelength, bandwidth and type of filter, and returns a filter with the given features; "applyFilter" receives a spectrum and a filter, and returns a scalar representing the filter response on that spectrum; "performCrossValidation" receives a regressor, the sets X and y, the number of folds for k-fold cross validation and the random number generator's seed for fold partition, and returns the average R^2 result from the cross validation.

Function g:

$F1, F2, F3, F4 \leftarrow$ input; four COTS filters

$X \leftarrow$ an empty set
$y \leftarrow$ the set of dry matter values of all the samples

for *each spectrum from the raw spectra* **do**
    $x1 \leftarrow$ applyFilter($spectrum, F1$)
    $x2 \leftarrow$ applyFilter($spectrum, F2$)
    $x3 \leftarrow$ applyFilter($spectrum, F3$)
    $x4 \leftarrow$ applyFilter($spectrum, F4$)

    The set $\{x1, x2, x3, x4\}$ is added to X as a new sample
end

scores $\leftarrow$ an empty set

for *each* $i \in \{1, 2, 3, 4, 5\}$ **do**
    regressor $\leftarrow$ an ε-SVM is set up as regressor
    $R^2 \leftarrow$ performCrossValidation($regressor, X, y, folds = 5, seed = i$)
    R^2 is added to *scores*
end

fitness $\leftarrow$ average($scores$)

return *fitness*

Algorithm 2: Implementation of the fitness function g, that receive four commercial off-the-shelf filters. The function "applyFilter" receives a spectrum and a filter, and returns a scalar representing the filter response on that spectrum; "performCrossValidation" receives a regressor, the sets X and y, the number of folds for k-fold cross validation and the random number generator's seed for fold partition, and returns the average R^2 result from the cross validation.